Electronic Supplementary Information for

AIEgens modulated per-functionalized flower-like IRMOF-3 frameworks with tunable light emission and excellent sensing properties

Xujie Li[§,a], Siqi Xie[§,a], Yuanzhuo Hu[a], Jun Xiang[c], Lumin Wang[a], Ruili Li[a], Miao Chen[a, b],

Fangbin Wang[c], Qi Liu[*,a, c] and Xiaoqing Chen[*,a]

[a]*College of Chemistry and Chemical Engineering, the Hunan Provincial Key Laboratory of Water Environment and Agriculture Product Safety, Central South University, Changsha 410083, Hunan, China.*
[a]*College of Life Science, Central South University, Changsha 410083, Hunan, China.*
Hunan Institute of Food Quality Supervision Inspection and Research, the Hunan Provincial Key
[c]*Laboratory of Food Safety Monitoring and Early Warning, Changsha 410083, Hunan, China.*
E-mail address: iliuqi@csu.edu.cn, xqchen@csu.edu.cn
[§]*X.-J. L. and S.-Q. X. contributed equally to this work.*

Table of contents

1. General information

Ultrapure water was prepared with a resistivity of 18.25 MΩ·cm^{-1} by a Molecular water purification system. Unless otherwise noted, all the reagents were purchased from commercial suppliers and used without further purification.

The field emission scanning electron microscopy (FTSEM) image was recorded on a Nova Nano SEM 430 field emission gun scanning electron microscope. The thermal gravimetric analysis (TGA) was performed under a N_2 atmosphere from 30 to 1000 ℃ at a Mattler Toledo TGA-SDTA851 with a flow rate of 50 mL/min and heating rate of 10 ℃/min, between 30 to 1000 °C. Brunauer–Emmett–Teller (BET) surface area was measured at 77 K using Micromeritics (TriStar 3020). UV-Vis absorption spectra were recorded on a Shimadzu UV-2600 UV-Vis spectrophotometer. Fourier transform infrared (FT-IR) spectra were obtained on an ErkinElmer SP-2 spectrometer. The fluorescence measurement was conducted on a PerkinElmer LS 55 spectrophotometer equipped with a 1×1 cm^2 quartz cell. The fluorescent lifetime and absolute fluorescence quantum yield (QY) of LMOFs were obtained using the timecorrelated single-photo counting (TCSPC) system on Horiba Scientific QM-8075. NMR spectra were recorded on Bruker AVANCE III 400 NMR spectrometer. ^{1}H NMR spectra were recorded at 400 MHz. The chemical shifts were recorded in parts per million (ppm, δ) relative to tetramethylsilane and with the solvent resonance as the internal standard. Data were reported as follows: chemical shift, multiplicity (s =singlet, d =doublet, t =triplet, q =quartet, m =multiplet), coupling constants (Hz), integration. ^{13}C NMR data were collected at 100 MHz with complete proton decoupling. Chemical shifts were reported in ppm from the tetramethylsilane with the solvent resonance as internal standard. High resolution mass spectroscopy (HRMS) was recorded on TOF MS ES+ mass spectrometer, and methanol were used to dissolve the sample. The powder X-ray diffraction (PXRD) patterns were taken using a Rigaku diffractometer in the 2θ range 5–50° with step width of 0.05°.

2. Preparation and characterization of Schiff-base 3a-3j.

2.1 Two-step synthesis of the Schiff-base 3a-3j and IRMOF-3-(a-j).

Schiff-base condensation between an amine and an aldehyde is one of the most common reactions with mild reaction conditions, high yield and easy separation. The ATA: SAL molar ratio of 1:1.1 by optimizing the material ratio. Typically, ATA (0.181 g, 1 mmol) and NaOH (0.008 g, 0.2 mmol) was dispersed in 15 mL of methanol by sonication for 10 min, and then SAL (128 μL, 1.2 mmol) in 15 mL of methanol was added. The mixture was allowed to react at room temperature for 2 h with stirring, during the solution changed from being a clear solution to red precipitate. The product Schiff-base was filtered, washed with 15 mL alkaline methanol (0.1 mmol NaOH) to remove the remaining reactant and then dried under vacuum for 12 h at 60 °C in an oven to get the Schiff-base powder (0.231 g, Conversion: 81 %). After drying under vacuum, the pure product was obtained. General Method for the preparation of other derivatives.

Schiff-base (0.28 g, 1.0 mmol) was dispersed in 15 mL of H_2O: methanol (v/v, 1/1) by stirring for 10 min, and then added $Zn(NO_3)_2 \cdot 6H_2O$ (0.45 g, 1.5 mmol) in the reaction solution. Initially, the reaction solution was transparent indicating complete dissolution of monomers. As the coordination reaction proceeded, the solution became opaque indicating the formation of MOF particles. After stirring for 6 hours, the product started to precipitate from the suspension. Finally, the reaction solution with almost clear supernatant was obtained after 24 hours. The mixture was allowed to react at room temperature for 24 h with stirring, after the solution being changed from a clear solution to yield yellow-green precipitates, the product MOF was filtered, collected by centrifugation at 8000 rpm for 3 min, washed three times with methanol to remove the remaining reactant and then dried under vacuum for 12 h at 60 °C in an oven to get the powder (0.16 g). Finally, the MOFs was stored at room temperature for further use.
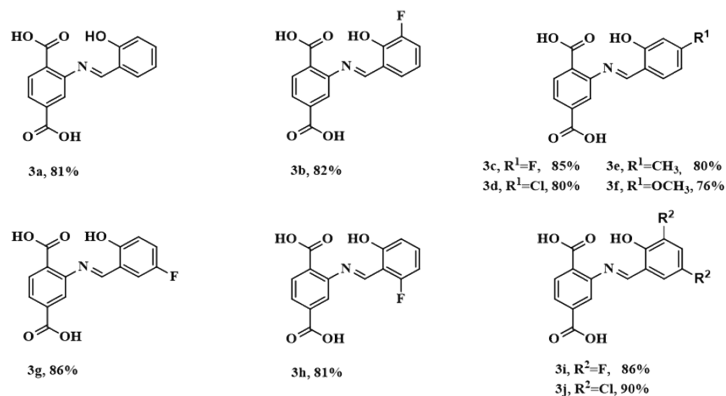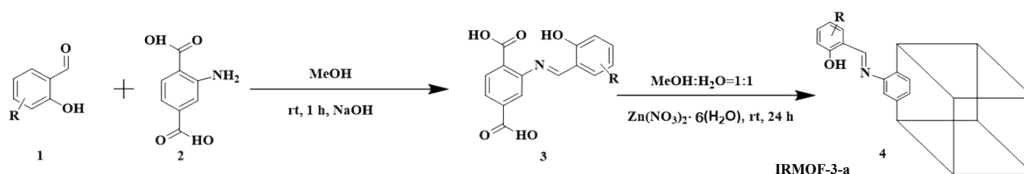
Figure S1: Two-step synthesis of the IRMOF-3-(**a-j**) and yield of Schiff-base **3a-3j**.

2.2 characterization of Schiff-base 3a.

2-[(2-hydroxy benzylidene) amino] terephthalic acid (Schiff-base **3a**). Orange powder, 81% yield; ^{1}H NMR (400 MHz, Deuterium Oxide) δ 9.88 (s, 1H), 7.69-7.71 (m, 1H), 7.64 (d, $J = 8.0$ Hz, 1H), 7.55-7.59 (m, 1H), 7.20-7.21 (m, 1H), 7.13 (dd, J = 1.6, 8 Hz, 1H), 7.05 (t, J = 7.6 Hz, 1H), 6.96 (d, J = 8.4 Hz, 1H); ^{13}C NMR (100 MHz, Deuterium Oxide) δ 197.84, 175.58, 175.30, 160.18, 147.20, 139.48, 137.57, 133.76, 130.75, 122.95, 121.11, 120.42, 117.98, 117.83, 117.19; HRMS (ESI): $[C_{15}H_{11}NO_5+H]^+$ Calcd 286.0710, Found 286.0714 $[M+H]^+$.
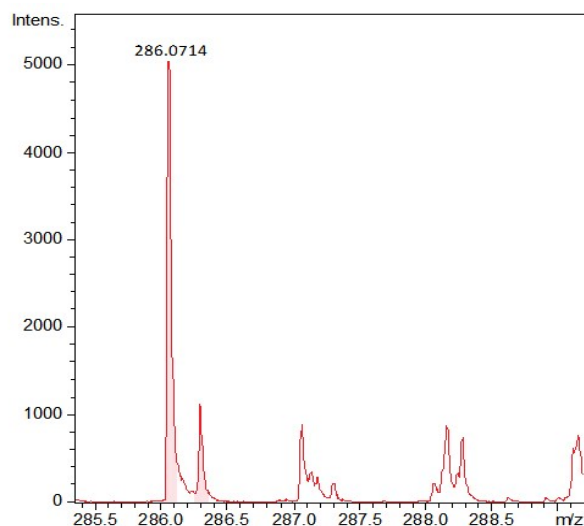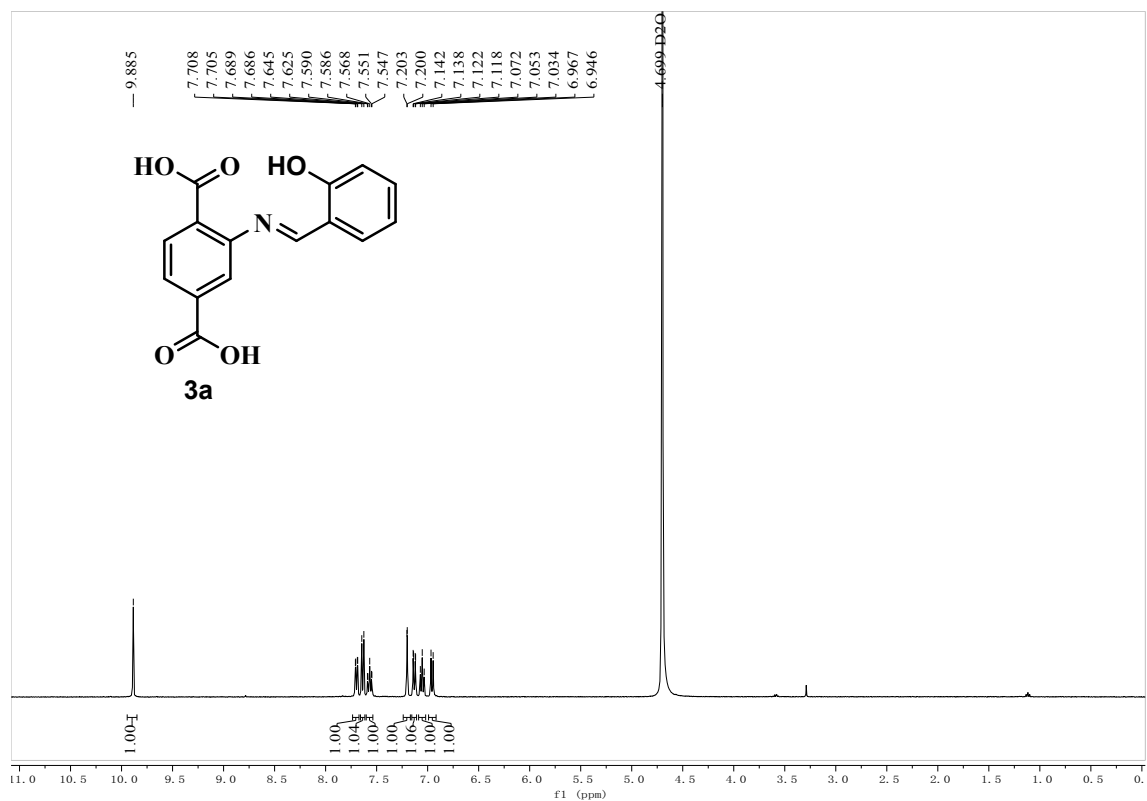

Figure S2: ESI-MS spectrum of product 3a.

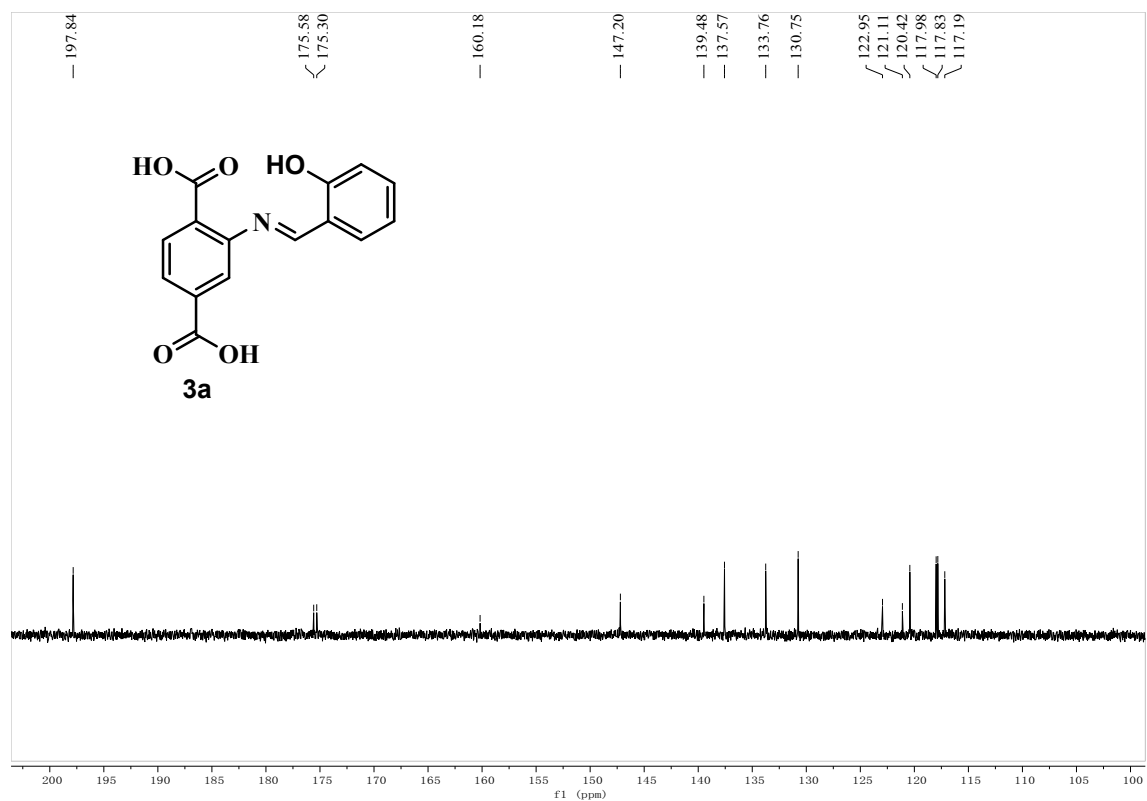Figure S3: ^{1}H NMR (400 MHz, Deuterium Oxide) spectrum of product 3a.

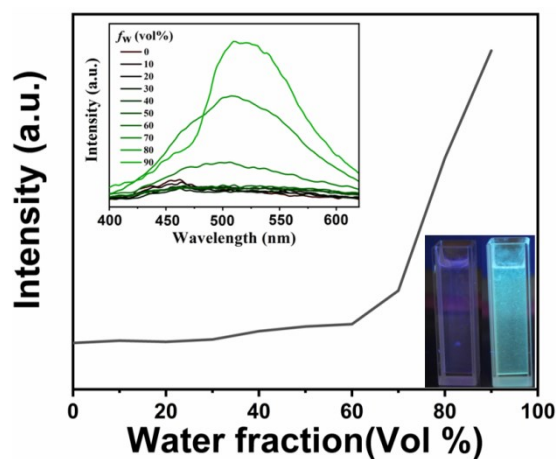Figure S4: ^{13}C NMR (100 MHz, Deuterium Oxide) spectrum of product 3a.

Figure S5. The typical AIE phenomenon of Schiff-base **3a**.
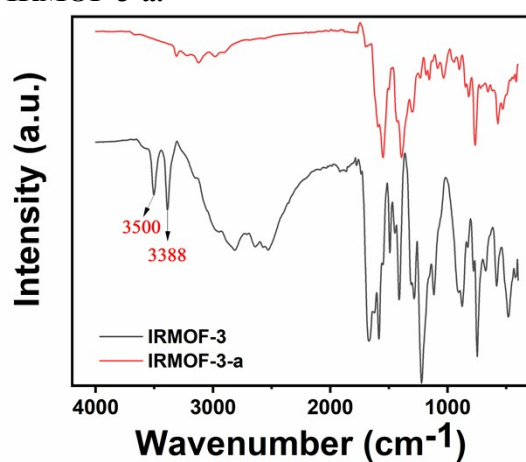
2.3 characterization of IRMOF-3-a.

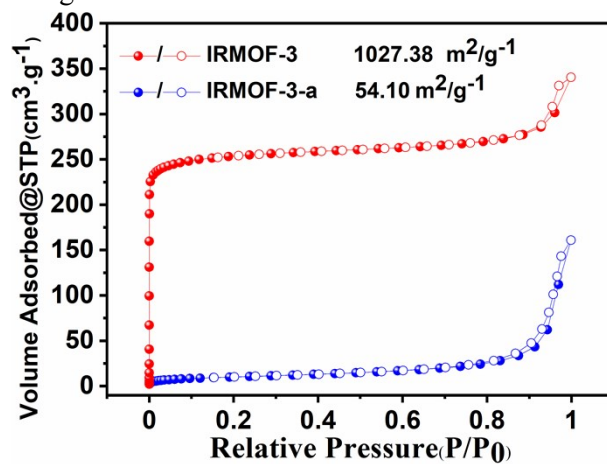Figure S6. The FTIR image of IRMOF-3 and IRMOF-3-**a**.

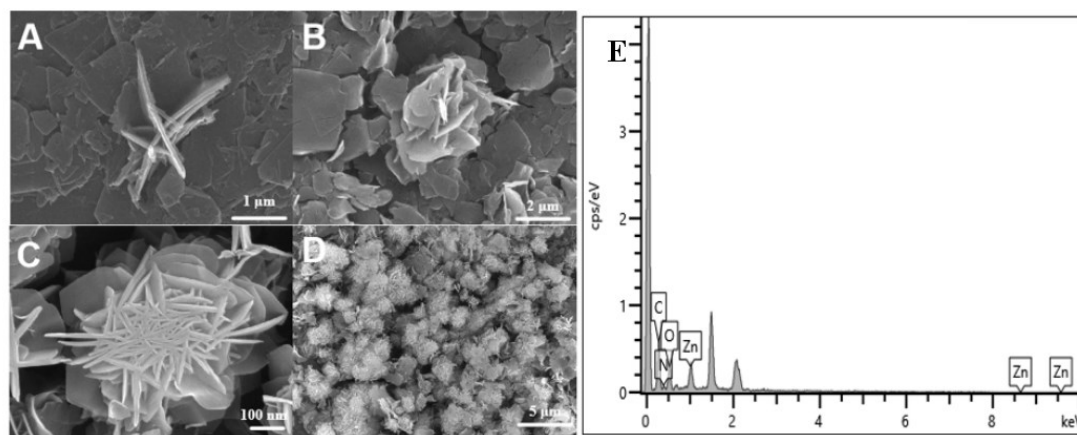Figure S7. N_2 isotherms of IRMOF-3 and IRMOF-3-**a**.

Figure S8. The self-assembly growth process: (A)1 h, (B) 6 h, (C)24 h, (D) low-magnification FTSEM image of IRMOF-3-**a**. (E) Energy dispersive X-ray spectrum (EDS) of IRMOF-3-**a**.
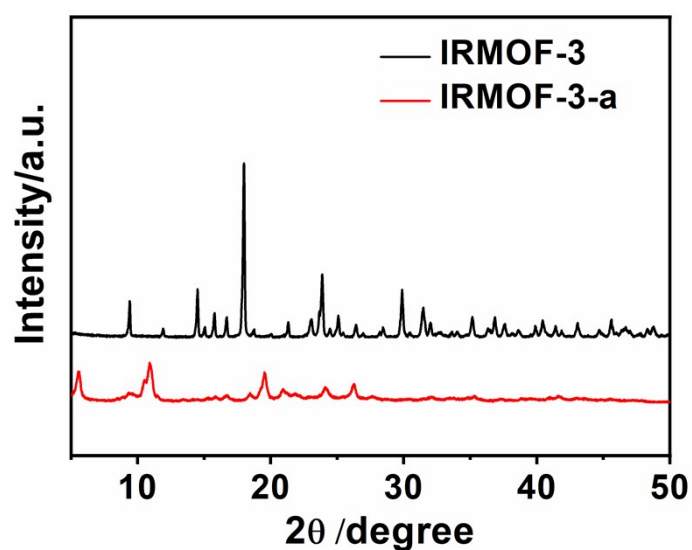

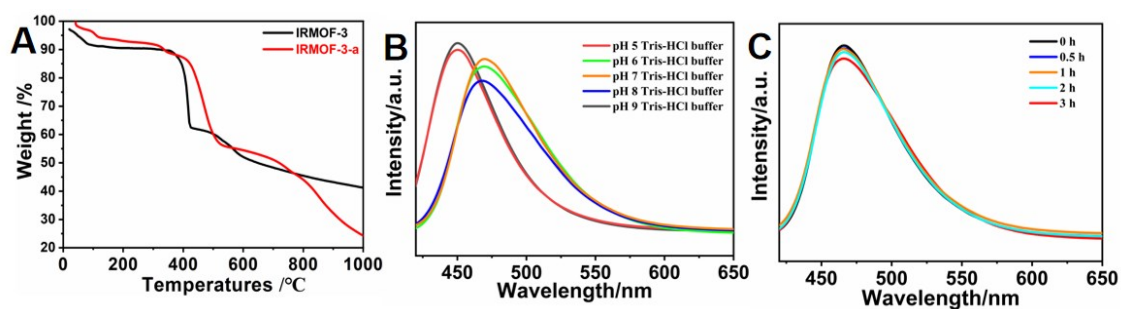Figure S9. The PXRD image of IRMOF-3 and IRMOF-3-**a**.

Figure S10. The thermogravimetric analysis image of IRMOF-3 and IRMOF-3-**a**.
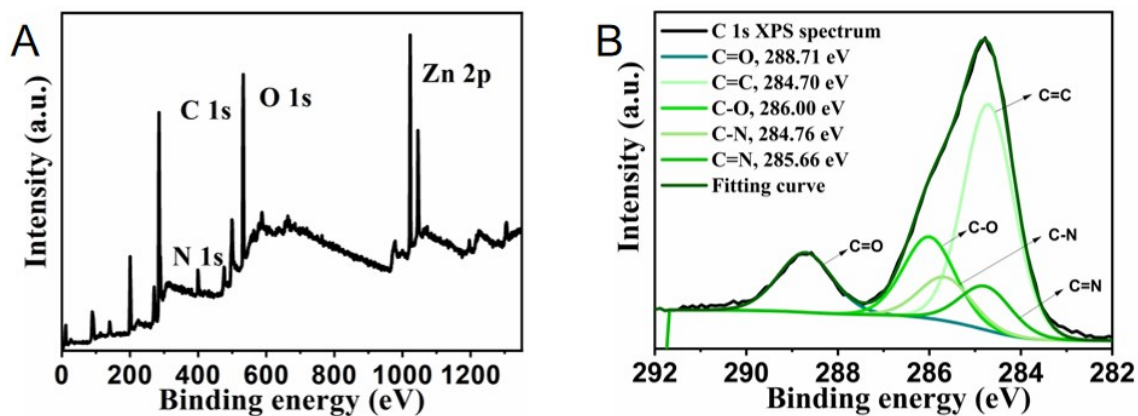
Figure S11. (A) XPS spectrum. (B) C 1s XPS spectrum of IRMOF-3-**a**. Non-oxygenated ring C (C=C) group (284.70 eV, 48.78%), C-O group (286.00 eV, 18.05%), C=O group (288.71 eV, 13.66%), C-N group (285.66 eV, 9.76%), and C-N group (284.76 eV, 9.76%).

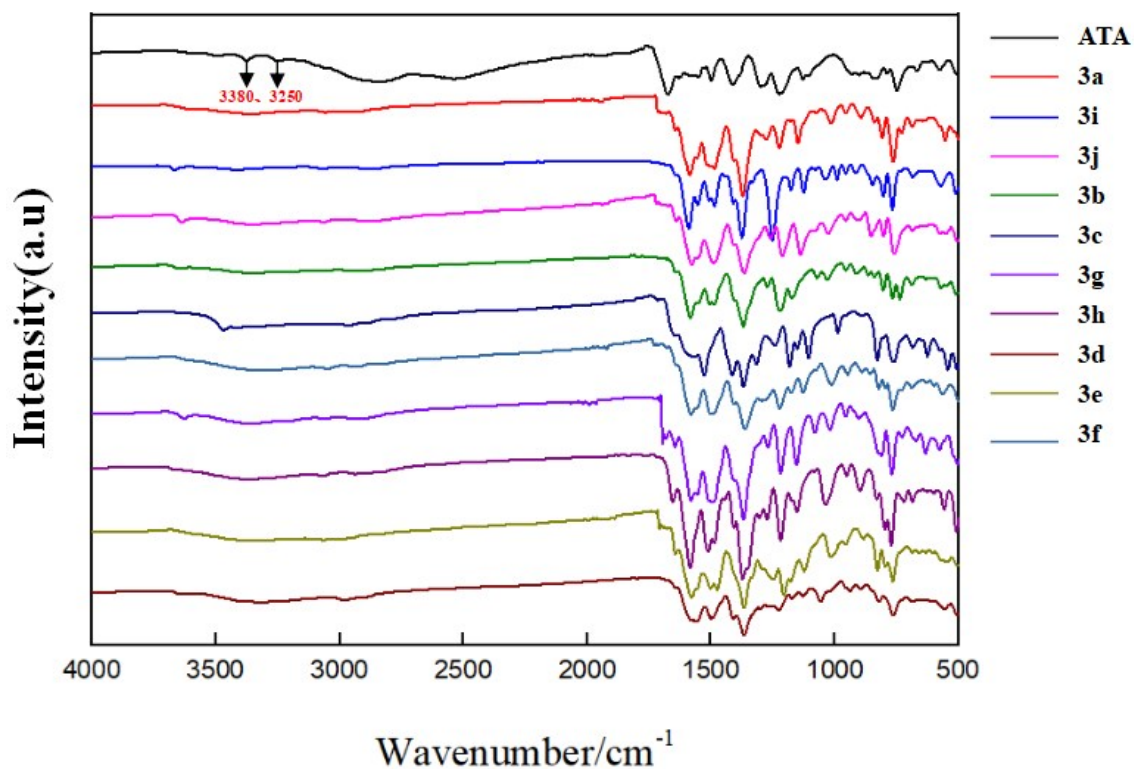**2.4 characterization of Schiff-base 3b-3j.**

Figure S12: FT-IR spectra of ATA and schiff base **3a-3j**.

Characterization date of Schiff-base **3b**, jacinth powder, 82% yield, ^{1}H NMR (400 MHz, CD$_3$OD:D$_2$O1:1) δ 9.86 (s, 1H), 7.51 (d, J = 8.0 Hz, 1H), 7.07 – 7.11 (m, 2H), 6.97 – 7.02 (m, 2H), 6.22 (m, 1H);

^{13}C NMR (100 MHz, CD$_3$OD:D$_2$O 1:1) δ 193.53 , 175.43 , 175.05 , 163.42 , 163.28 , 158.03 , 155.66 , 147.32 , 139.39 , 130.72 (d, J = 7.0 Hz) , 126.44 (d, J = 5.2 Hz), 123.76 – 123.88 (m), 122.72, 120.87 – 121.13 (m), 120.87 – 121.13 (m), 117.71 – 117.85 (m), 111.84 – 111.94 (dd, J = 7.0, 2.8 Hz);

HRMS (ESI): [C$_{15}$H$_{10}$FNO$_5$+H]$^+$ Calcd 304.0616, Found 304.0619 [M+H]$^+$.
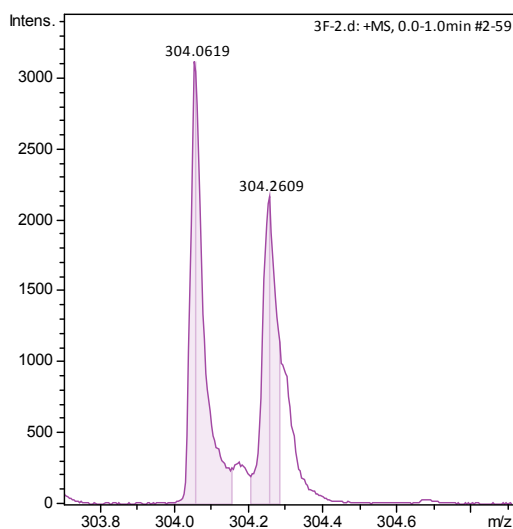
Figure S13: ESI-MS spectrum of product 3b.
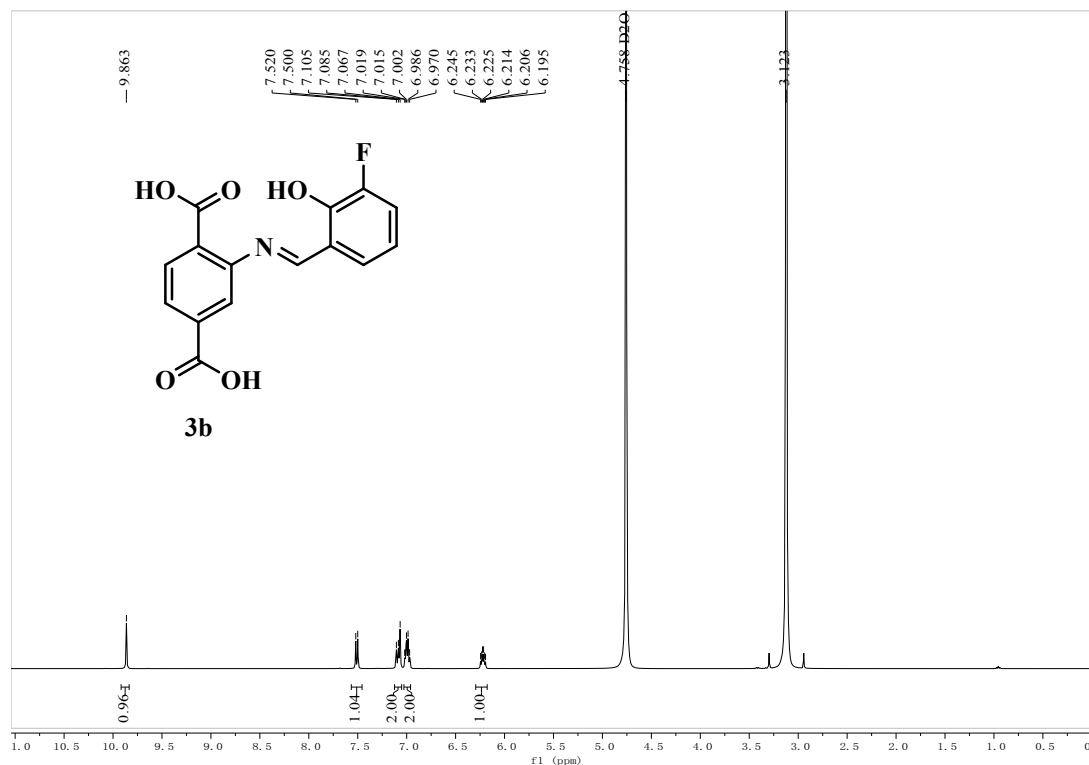
Figure S14: ^{1}H NMR (400 MHz, CD$_3$OD:D$_2$O 1:1) spectrum of product 3b.
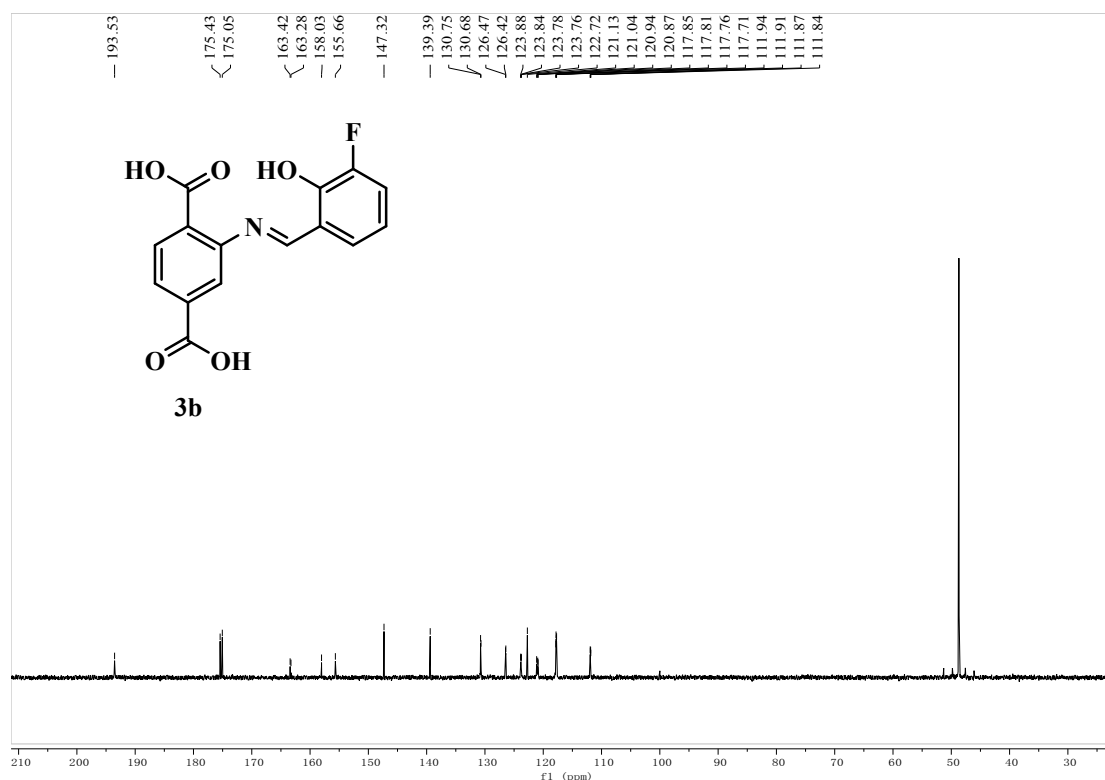
Figure S15: ^{13}C NMR (100 MHz, CD$_3$OD:D$_2$O 1:1) spectrum of product 3b.

Characterization date of Schiff-base **3c**, jacinth powder, 85% yield, ^{1}H NMR (400 MHz, CD$_3$OD:D$_2$O 1:1) δ 9.45 (s, 1H), 7.32 (d, J = 8.0 Hz, 1H), 7.10 (t, J = 8.4 Hz, 1H), 6.87 (d, J = 1.2 Hz, 2H), 6.80 (dd, J = 1.6, 8.0 Hz, 1H), 5.87 – 5.93 (m, 2H);

^{13}C NMR (100 MHz, CD$_3$OD:D$_2$O 1:1) δ 175.60 , 175.29 , 147.27 , 139.48 , 131.04 , 130.74 , 122.94 , 117.93 , 117.80 , 107.75 (d, J = 17.0 Hz), 103.20 (d, J = 24.3 Hz);

HRMS (ESI): [C$_{15}$H$_{10}$FNO$_5$+Na]$^+$ Calcd 326.0435, Found 326.0438 [M+Na]$^+$.

Figure S16: ESI-MS spectrum of product 3c.
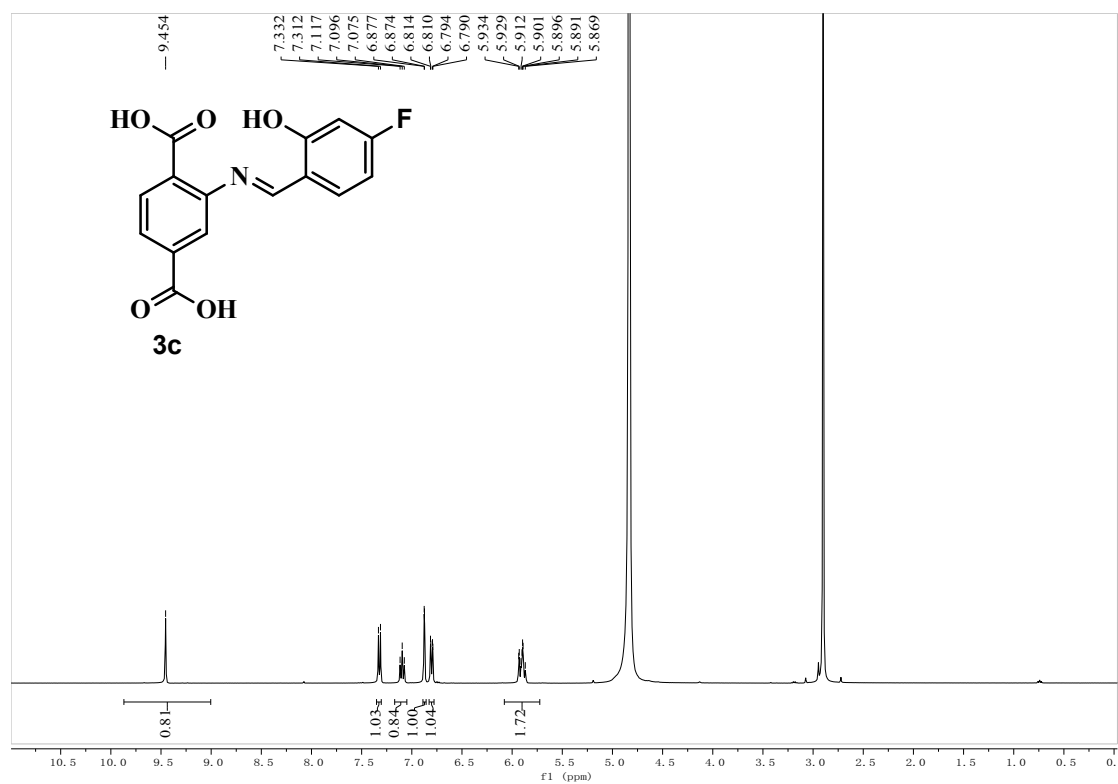
Figure S17: ^{1}H NMR (400 MHz, CD$_3$OD:D$_2$O 1:1) spectrum of product 3c.

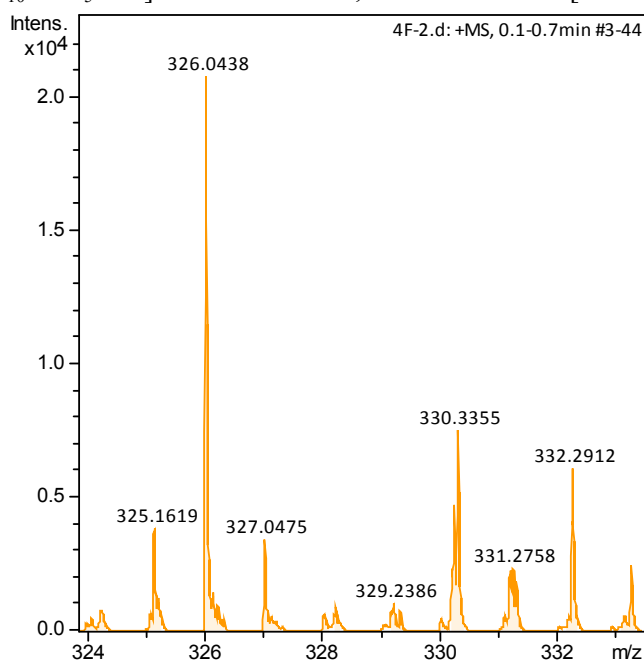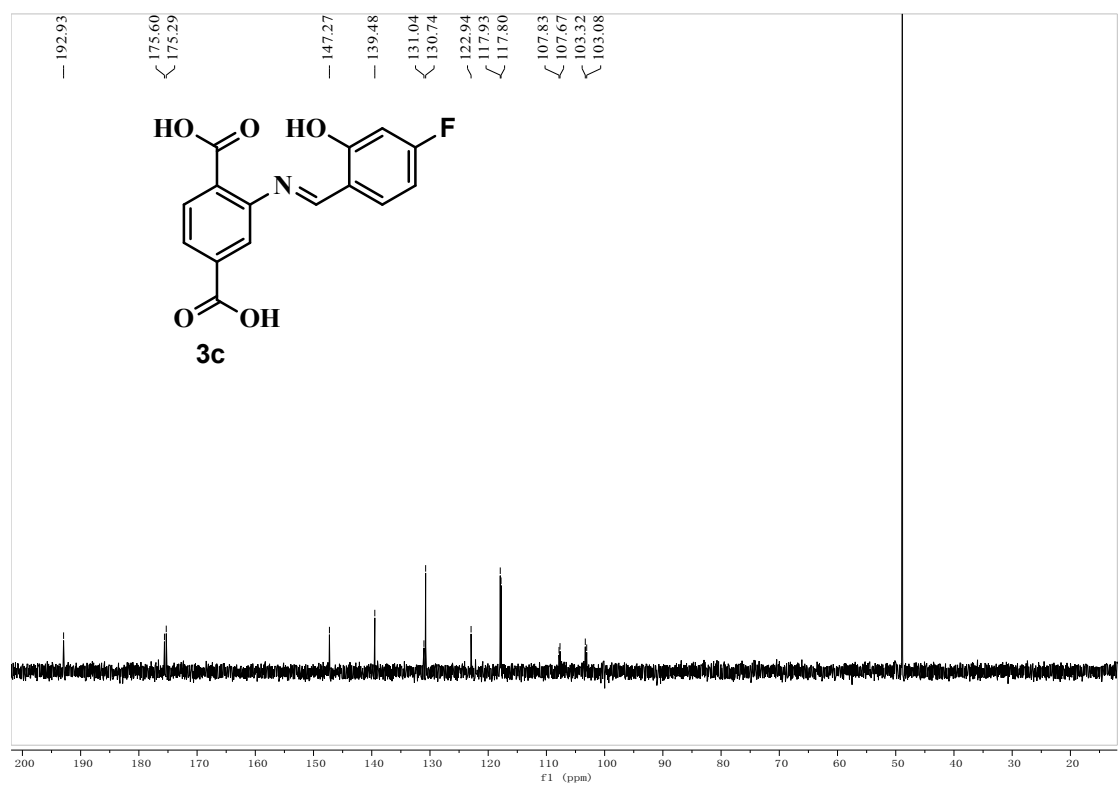Figure S18: ^{13}C NMR (100 MHz, CD$_3$OD:D$_2$O 1:1) spectrum of product 3c.

Characterization date of Schiff-base **3d**, orange powder, 80% yield, ^{1}H NMR (400 MHz, CD$_3$OD:D$_2$O 1:1) δ 9.91 (s, 1H), 7.62 (d, J = 8.0 Hz, 1H), 7.40 (d, J = 8.4 Hz, 1H), 7.18 (s, 1H), 7.11 (d, J = 7.6 Hz, 1H), 6.64 (s, 1H), 6.46 (d, J = 8.4 Hz, 1H);

^{13}C NMR (100 MHz, CD$_3$OD:D$_2$O 1:1) δ 193.62 , 175.61 , 175.29 , 174.51 , 147.28 , 143.02 , 139.47 , 130.75 , 129.92 , 123.44 , 122.93 , 122.75 , 117.92 , 117.80 , 114.57 ;

HRMS (ESI): [C$_{15}$H$_{10}$ClNO$_5$+Na]$^+$ Calcd 342.0140, Found 342.0144 [M+Na]$^+$.
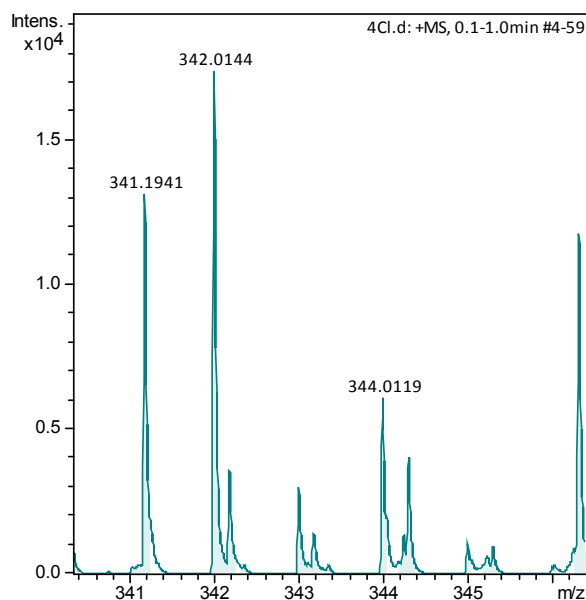
Figure S19: ESI-MS spectrum of product 3d.
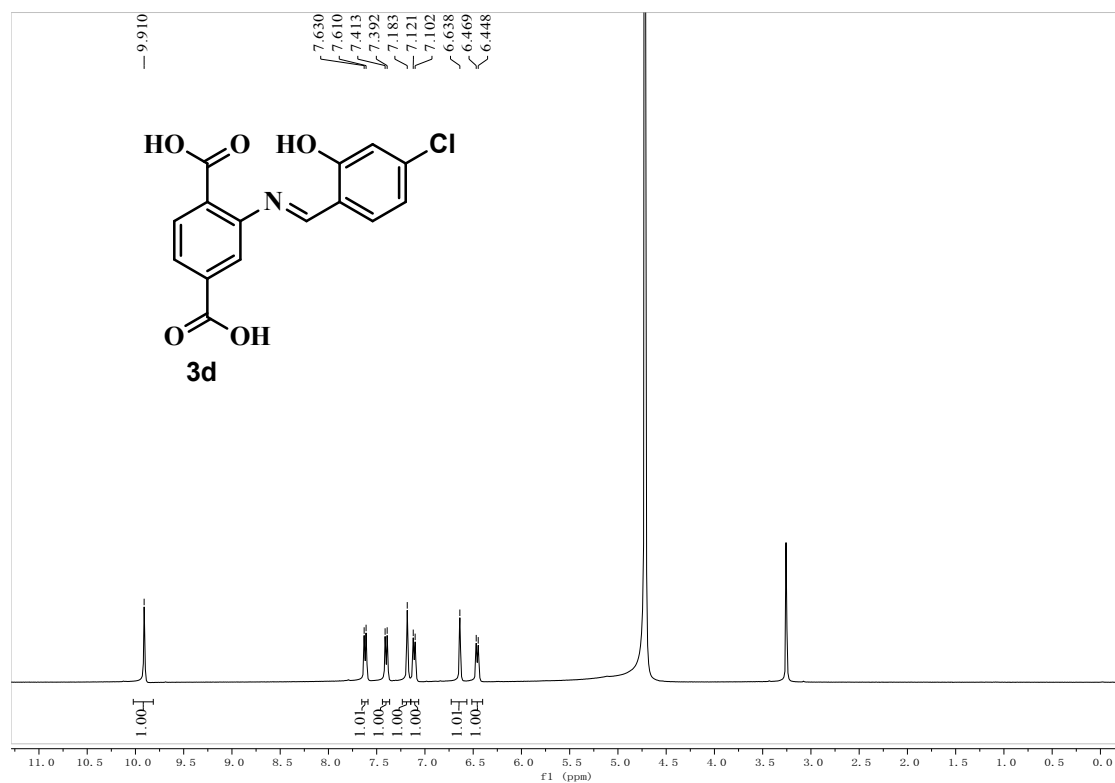
Figure S20: ^{1}H NMR (400 MHz, CD$_3$OD:D$_2$O 1:1) spectrum of product 3d.
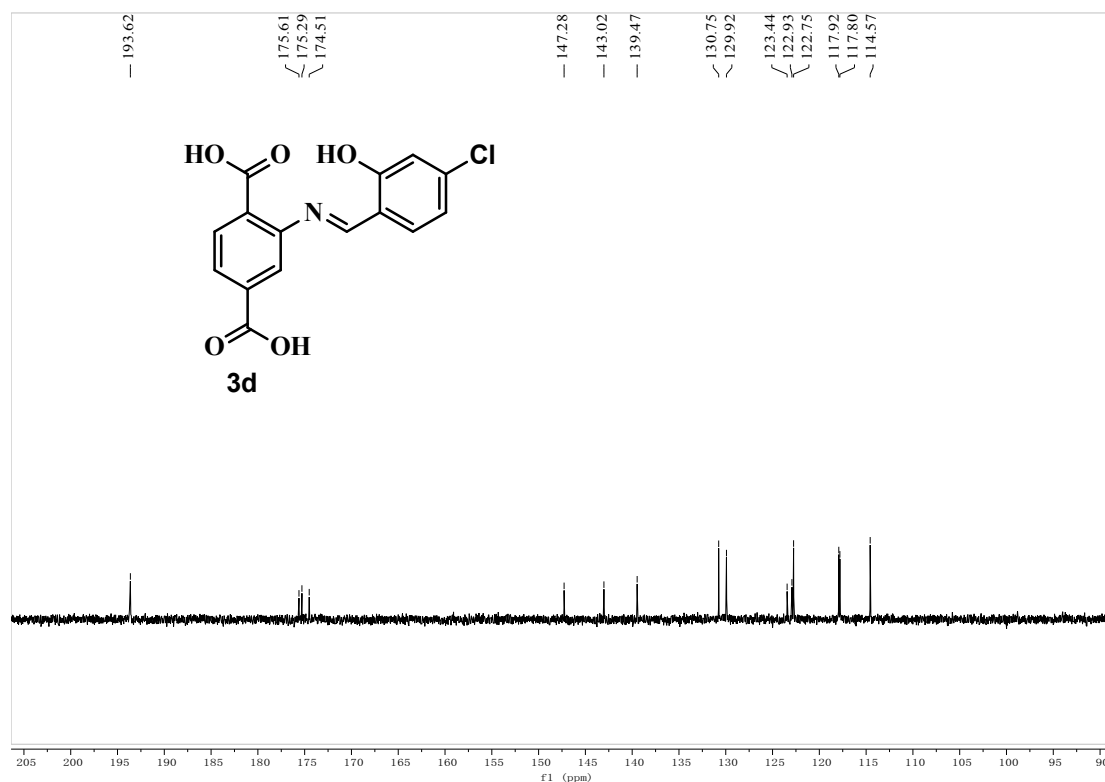
Figure S21: ^{13}C NMR (100 MHz, CD$_3$OD:D$_2$O 1:1) spectrum of product 3d.

Characterization date of Schiff-base **3e**, jacinth powder, 80% yield, ^{1}H NMR (400 MHz, CD$_3$OD:D$_2$O 1:1) δ 9.74 (s, 1H), 7.49 (d, J = 8.0 Hz, 1H), 7.23 (d, J = 8.4 Hz, 1H), 7.05 (s, 1H), 6.98 (d, J = 8.0 Hz, 1H), 6.32 (s, 1H), 6.21 (d, J = 8.0 Hz, 1H), 2.01(s, 3H);
^{13}C NMR (100 MHz, CD3OD:D2O 1:1) δ 193.51 , 175.44 , 175.08 , 174.56 , 149.91 , 147.27 , 139.36 , 130.76 , 128.62 , 123.10 , 122.73 , 122.20 , 117.80 , 117.64 , 115.88 , 21.13;
HRMS (ESI): [C$_{16}$H$_{13}$NO$_5$+H]$^+$ Calcd 300.0866, Found 300.0878 [M+H]$^+$.
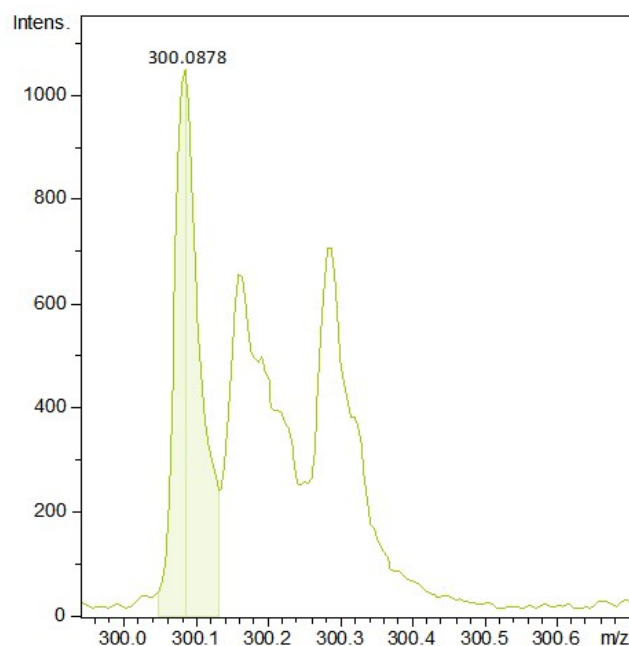
Figure S22: ESI-MS spectrum of product 3e.
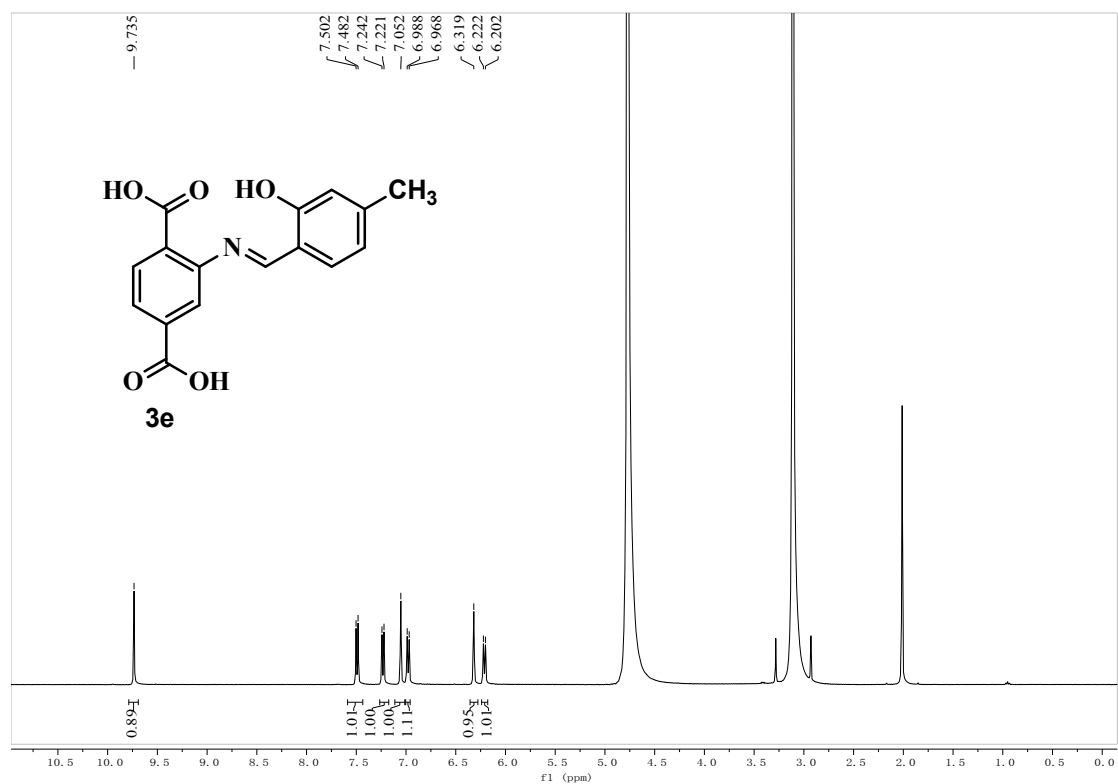
Figure S23: ^{1}H NMR (400 MHz, CD$_3$OD:D$_2$O 1:1) spectrum of product 3e.
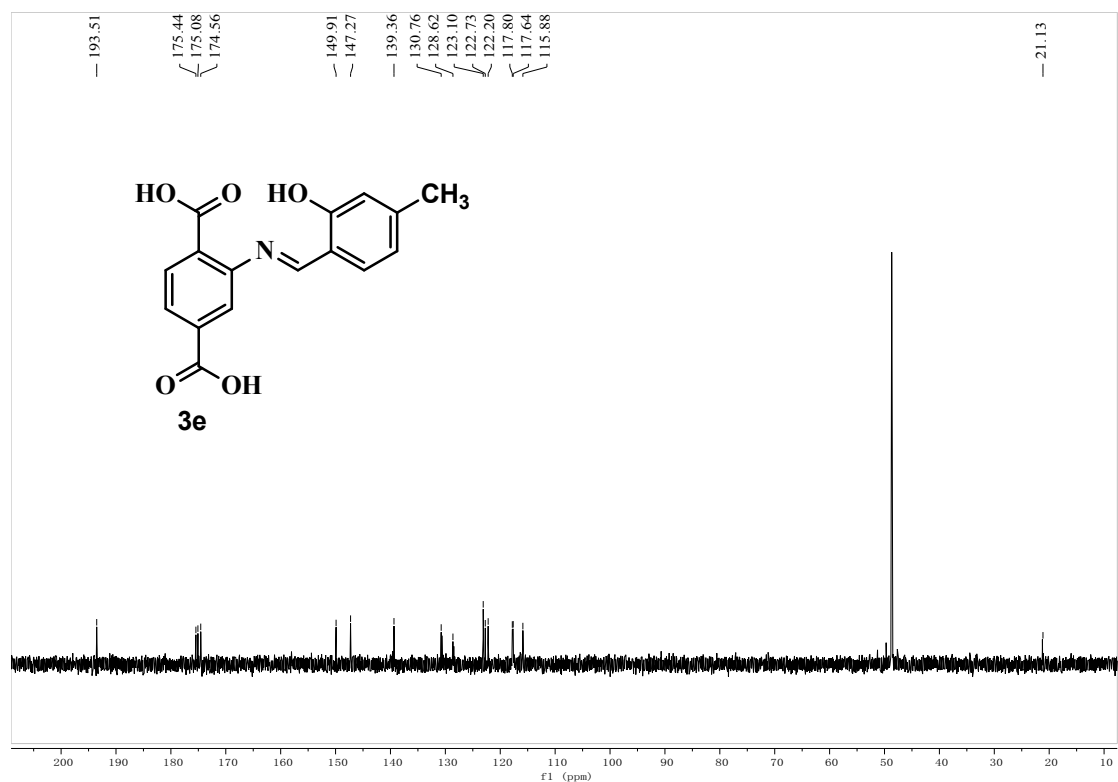
Figure S24: ^{13}C NMR (100 MHz, CD$_3$OD:D$_2$O 1:1) spectrum of product 3e.

Characterization date of Schiff-base **3f**, yellow powder, 76% yield, ^{1}H NMR (400 MHz, CD$_3$OD:D$_2$O 1:1) δ 9.73 (s, 1H), 7.60 (d, J = 8.4 Hz, 1H), 7.40 (d, J = 8.8 Hz, 1H), 7.16 (s, 1H), 7.09 (d, J = 8.0 Hz, 1H), 6.11 (d, J = 9.2 Hz, 1H), 6.06 (s, 1H), 3.71 (s, 3H);
^{13}C NMR (101 MHz, CD$_3$OD:D$_2$O 1:1) δ 191.77 , 177.16 , 175.59 , 175.27 , 167.56 , 147.27 , 139.45 , 130.74 , 130.12 , 122.91 , 119.35 , 117.90 , 117.77 , 104.85 , 104.10 , 55.27;
HRMS (ESI): [C$_{16}$H$_{13}$NO$_6$+Na]$^+$ Calcd 338.0635, Found 338.0640 [M+Na]$^+$.
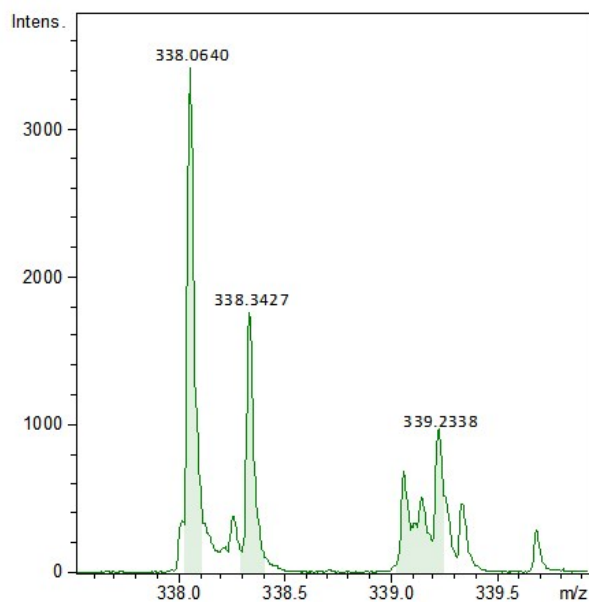
Figure S25: ESI-MS spectrum of product 3f.
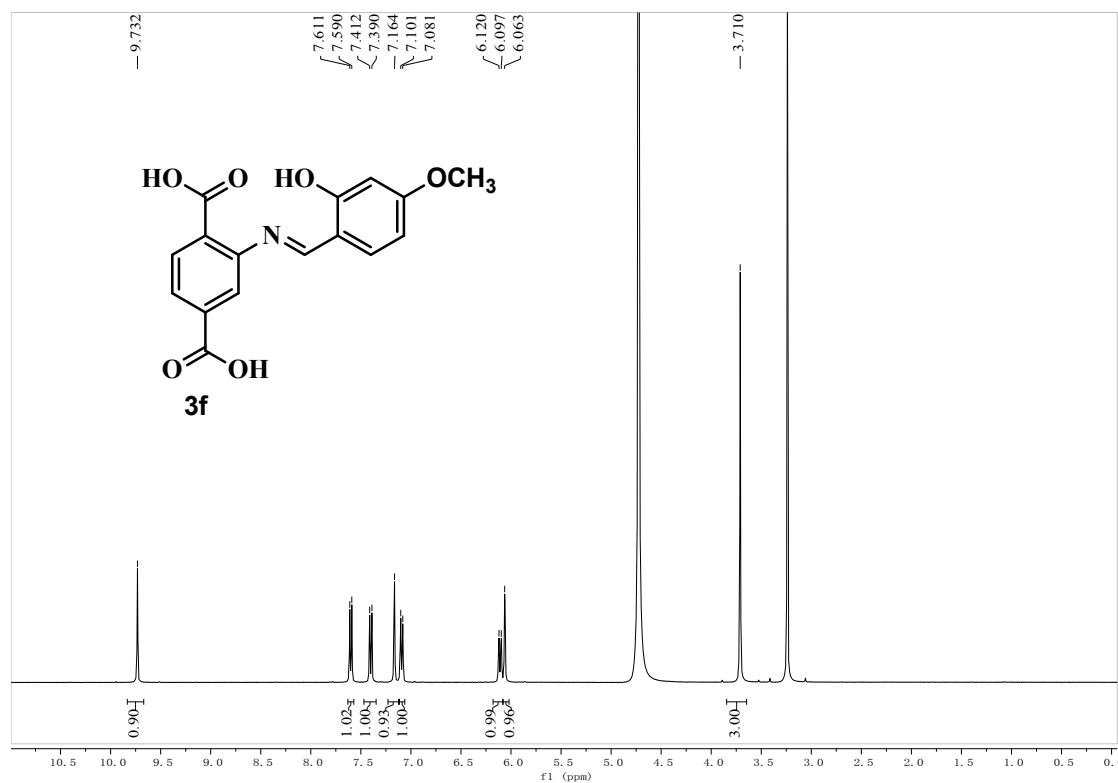
Figure S26: ^{1}H NMR (400 MHz, CD$_3$OD:D$_2$O 1:1) spectrum of product 3f.
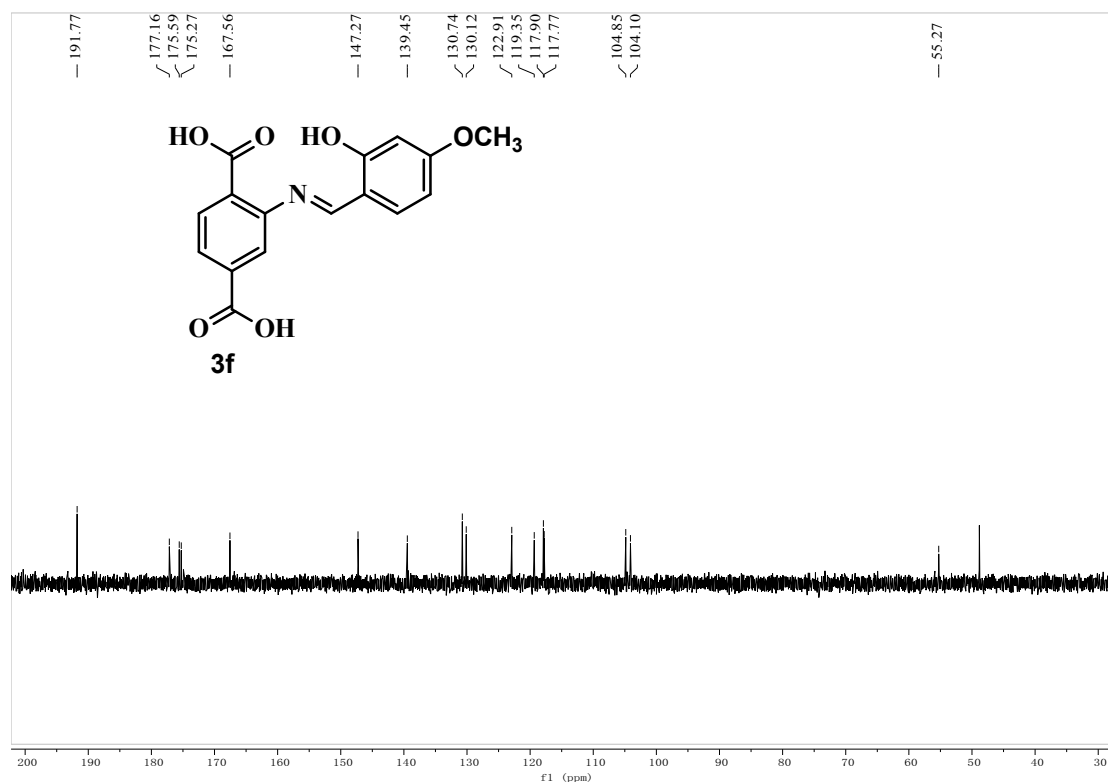
Figure S27: ^{13}C NMR (100 MHz, CD$_3$OD:D$_2$O 1:1) spectrum of product 3f.

Characterization date of Schiff-base **3g**, jacinth powder, 86% yield, ^{1}H NMR (400 MHz, Deuterium Oxide) δ 9.93 (s, 1H), 7.63 (d, J = 8.0 Hz, 1H), 7.41 (d, J = 3.2 Hz, 1H), 7.24 (dd, J = 2.8, 9.2 Hz, 1H), 7.19 (d, J = 1.2 Hz, 1H), 7.12 (dd, J = 1.2, 8.0 Hz, 1H), 6.60 (d, J = 9.2 Hz, 1H);

^{13}C NMR (100 MHz, Deuterium Oxide) δ 193.36 , 175.61 , 175.30 , 173.05 , 147.28 , 139.48 , 137.36 , 130.76 , 126.81 , 125.51 , 124.89 , 122.94 , 118.12 , 117.87 (d, J = 12.0 Hz);

HRMS (ESI): [C$_{15}$H$_{10}$FNO$_5$+Na]$^+$ Calcd 326.0435, Found 326.0435 [M+Na]$^+$.
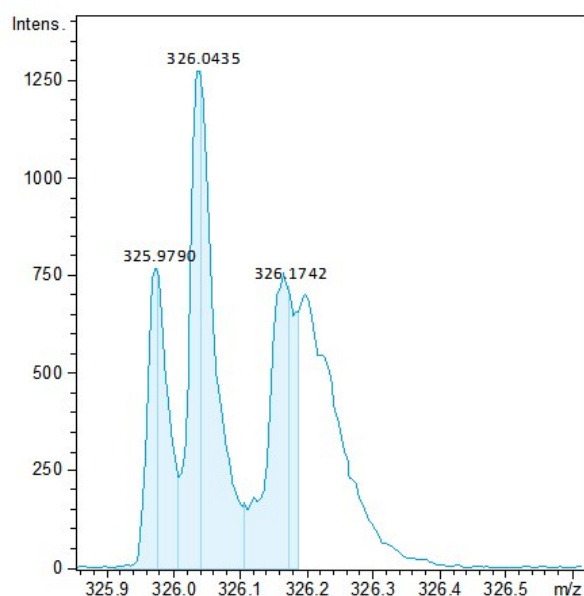
Figure S28: ESI-MS spectrum of product 3g.
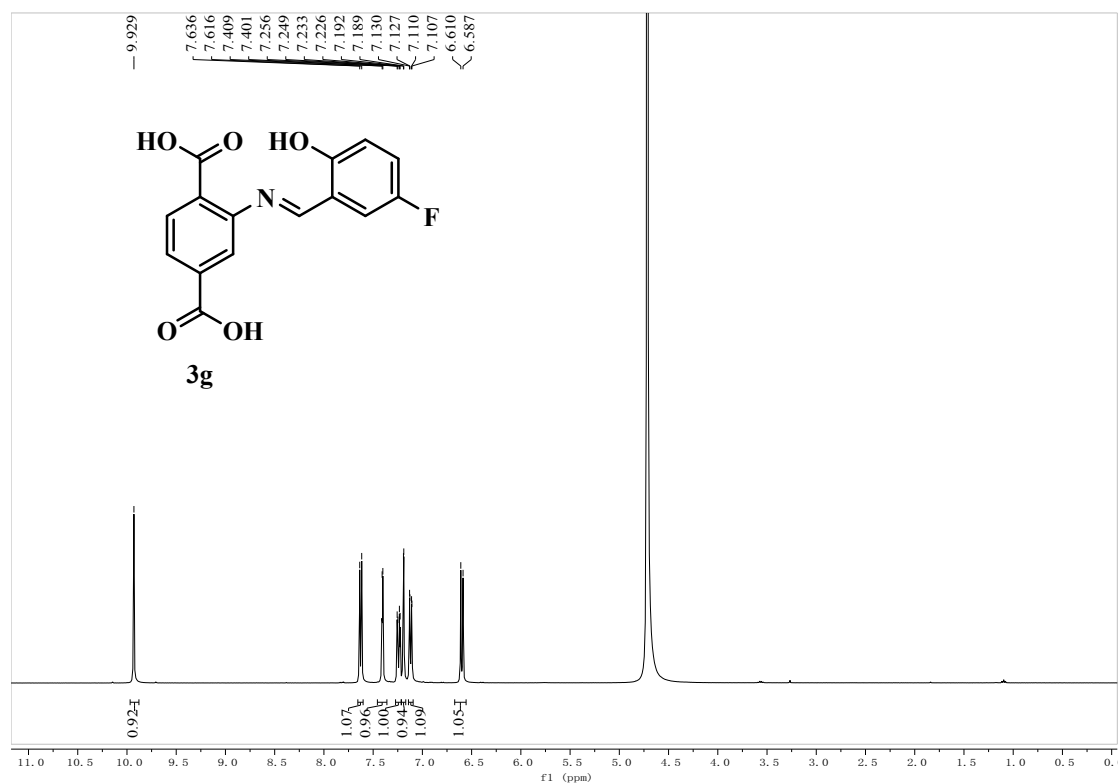
Figure S29: ^{1}H NMR (400 MHz, CD$_3$OD:D$_2$O 1:1) spectrum of product 3g.
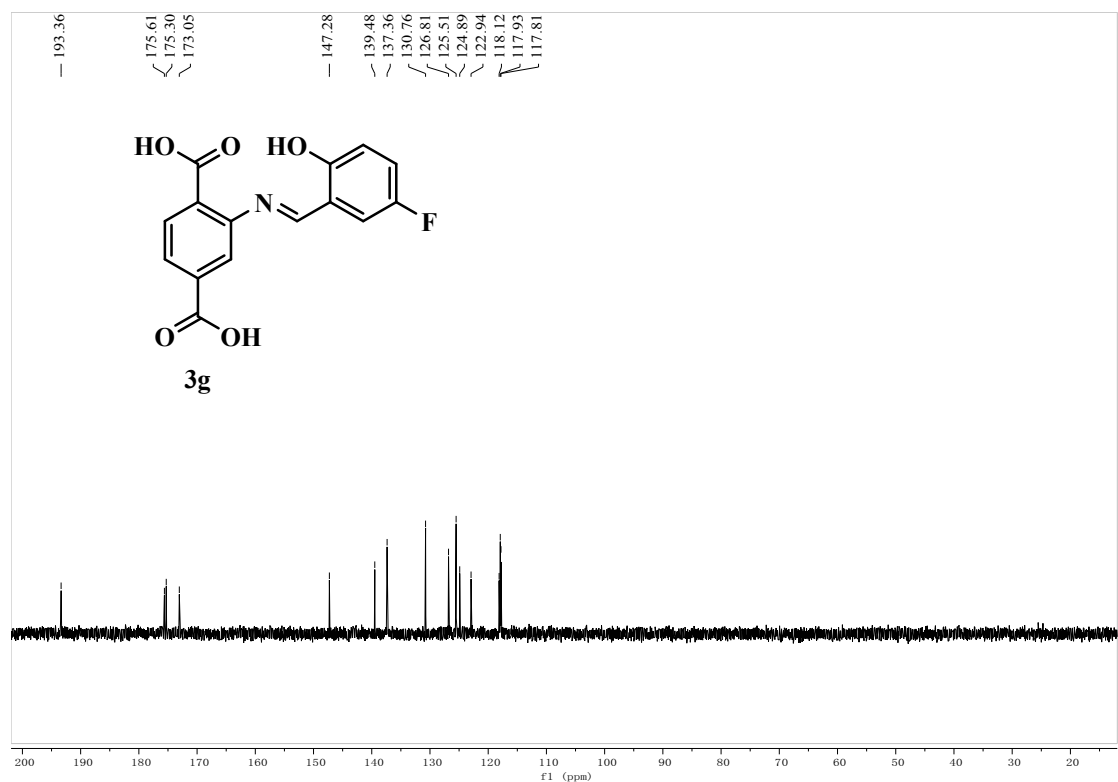
Figure S30: ^{13}C NMR (100 MHz, CD$_3$OD:D$_2$O 1:1) spectrum of product 3g.

Characterization date of Schiff-base **3h**, jacinth powder, 81% yield, ^{1}H NMR (400 MHz, CD$_3$OD:D$_2$O 1:1) δ 9.92 (s, 1H), 7.57 (d, J = 8.0 Hz, 1H), 7.13 – 7.21 (m, 2H), 7.06 (dd, J = 1.2, 8.0 Hz, 2H), 6.34 (d, J = 8.4 Hz, 1H), 6.06 (dd, J = 8.0, 12.0 Hz, 1H);

^{13}C NMR (100 MHz, CD$_3$OD:D$_2$O 1:1) δ 192.34 – 191.48 (m), 175.56 , 175.23 , 164.96 , 147.27 , 139.42 , 130.73 (d, J = 5.3 Hz), 122.86 , 119.08 (d, J = 2.8 Hz), 117.73 – 117.89 (m), 99.22 – 99.46 (m);

HRMS (ESI): [C$_{15}$H$_9$FNO$_5$+Na]$^+$ Calcd 326.0435, Found 326.0447 [M+Na]$^+$.

Figure S31: ESI-MS spectrum of product 3h.

Figure S32: ^{1}H NMR (400 MHz, CD$_3$OD:D$_2$O 1:1) spectrum of product 3h.

Figure S33: ^{13}C NMR (100 MHz, CD$_3$OD:D$_2$O 1:1) spectrum of product 3h.

Characterization date of Schiff-base **3i**, red powder, 86% yield, ^{1}H NMR (400 MHz, CD$_3$OD:D$_2$O 1:1) δ 10.01 (d, J = 3.2 Hz, 1H), 7.63 (d, J = 8.0 Hz, 1H), 7.19 (d, J = 1.2 Hz, 2H), 7.11 – 7.13 (m, 1H), 7.04 (ddd, J = 3.6, 8.8, 12.0 Hz, 1H), 6.93 – 6.96 (m, 1H);
^{13}C NMR (100 MHz, CD$_3$OD:D$_2$O 1:1) δ 192.62 – 192.78 (m), 175.61 , 175.30 , 151.27, 151.16, 147.28 , 139.48 , 130.76 , 122.94 – 124.18 (m) , 117.92 , 117.80 , 111.29 , 111.03 (d, J = 5.7 Hz), 110.77 , 106.24 (d, J = 3.9 Hz), 106.03 (d, J = 4.1 Hz);
HRMS (ESI): [C$_{15}$H$_9$F$_2$NO$_5$+Na]$^+$ Calcd 344.0341, Found 344.0341 [M+Na]$^+$.
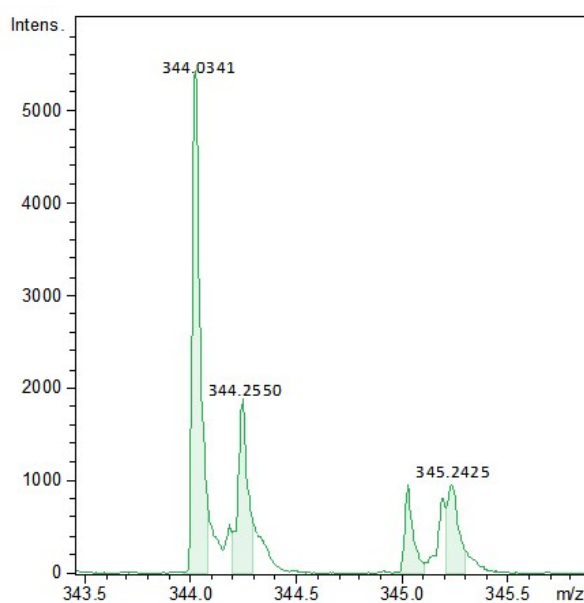
Figure S34: ESI-MS spectrum of product 3i.
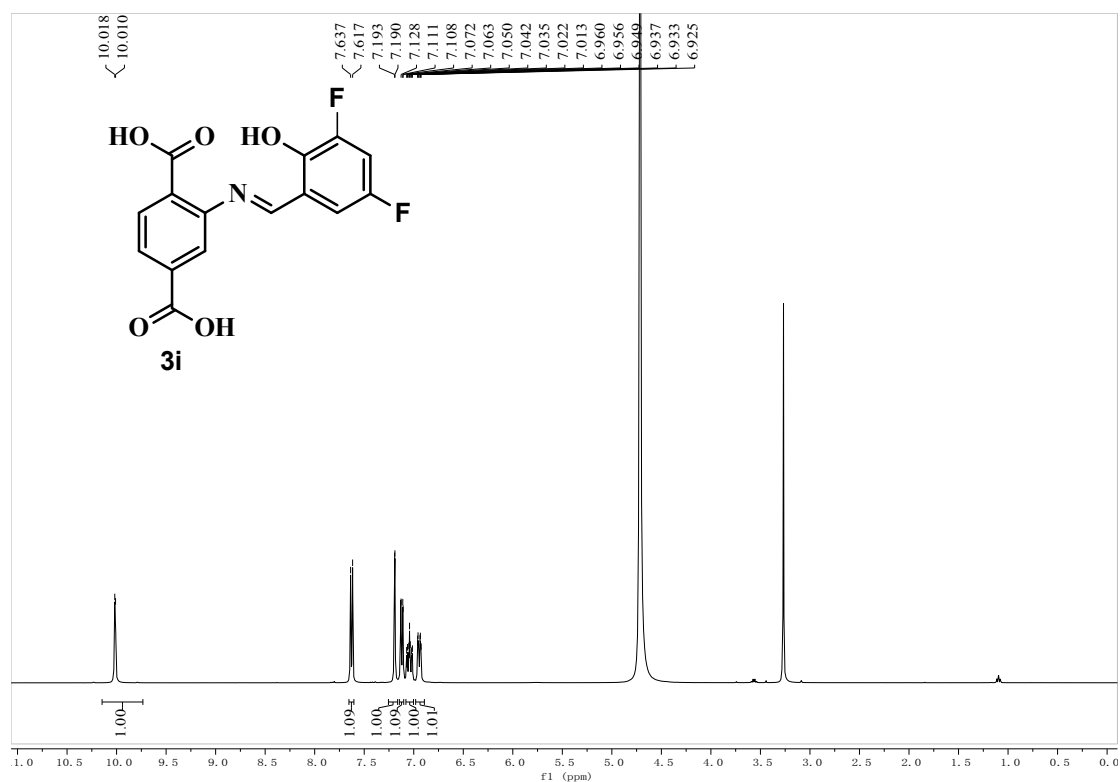
Figure S35: ^{1}H NMR (400 MHz, CD$_3$OD:D$_2$O 1:1) spectrum of product 3i.
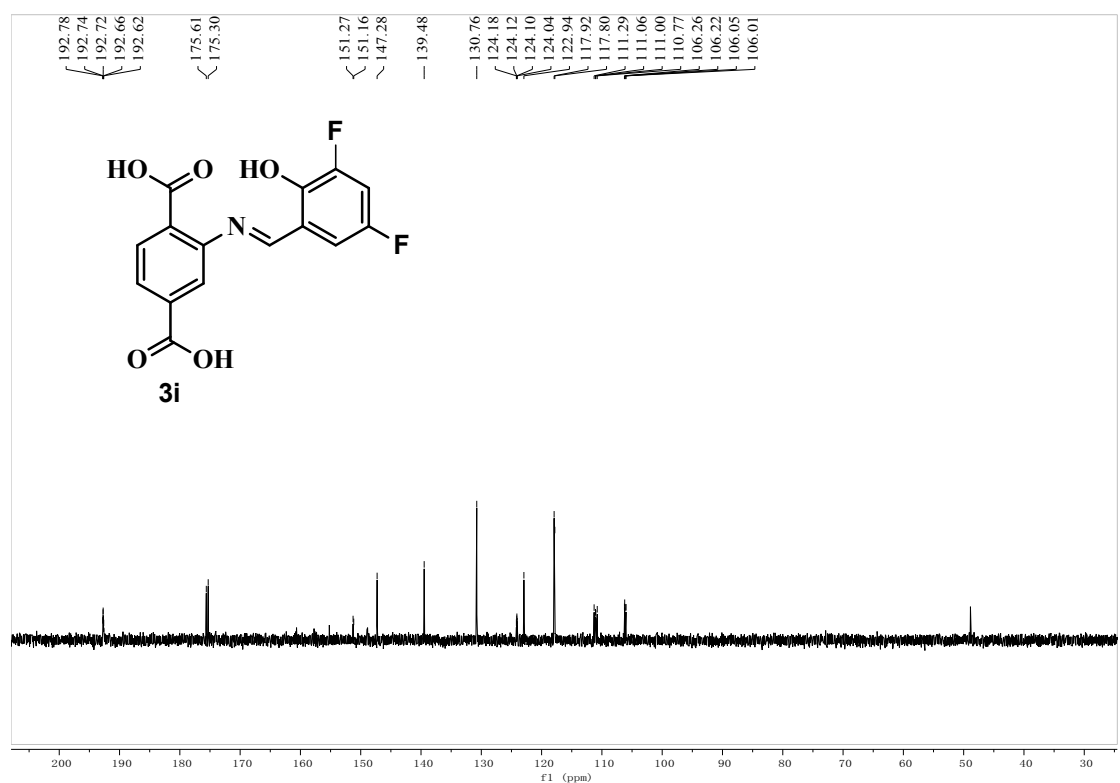
Figure S36: ^{13}C NMR (100 MHz, CD$_3$OD:D$_2$O 1:1) spectrum of product 3i.

Characterization date of Schiff-base **3j**, red powder, 90% yield, ^1H NMR (400 MHz, CD$_3$OD:D$_2$O 1:1) δ 9.91 (s, 1H), 7.59 (d, J = 8.0 Hz, 1H), 7.42 (s, 1H), 7.29 (s, 1H), 7.15 (s, 1H), 7.08 (d, J = 8.0 Hz, 1H);

^{13}C NMR (101 MHz, CD$_3$OD:D$_2$O 1:1) δ 175.58, 175.25 , 147.27 , 139.44 , 135.52 , 130.75 , 128.73 , 126.01 , 125.21 , 122.89 , 117.89 , 117.81 , 116.48 ;

HRMS (ESI):[C$_{15}$H$_9$Cl$_2$NO$_5$+Na]$^+$ Calcd 375.9750, Found 375.9741 [M+Na]$^+$.
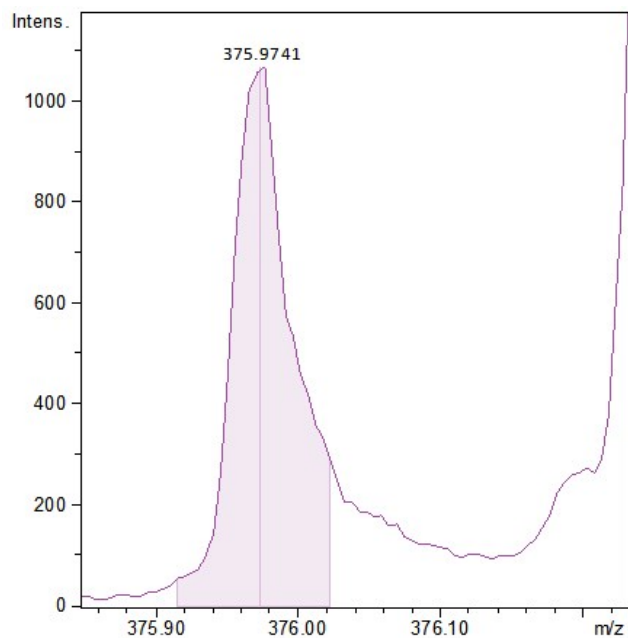
Figure S37: ESI-MS spectrum of product 3j.
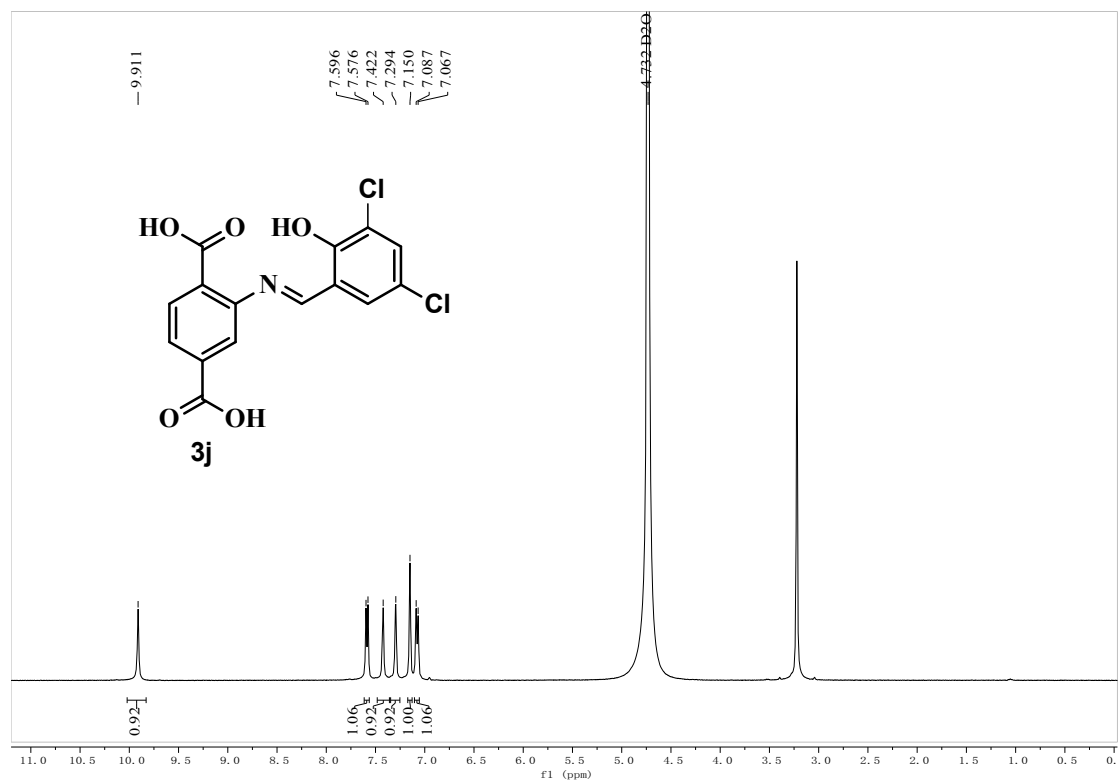
Figure S38: ^1H NMR (400 MHz, CD$_3$OD:D$_2$O 1:1) spectrum of product 3j.
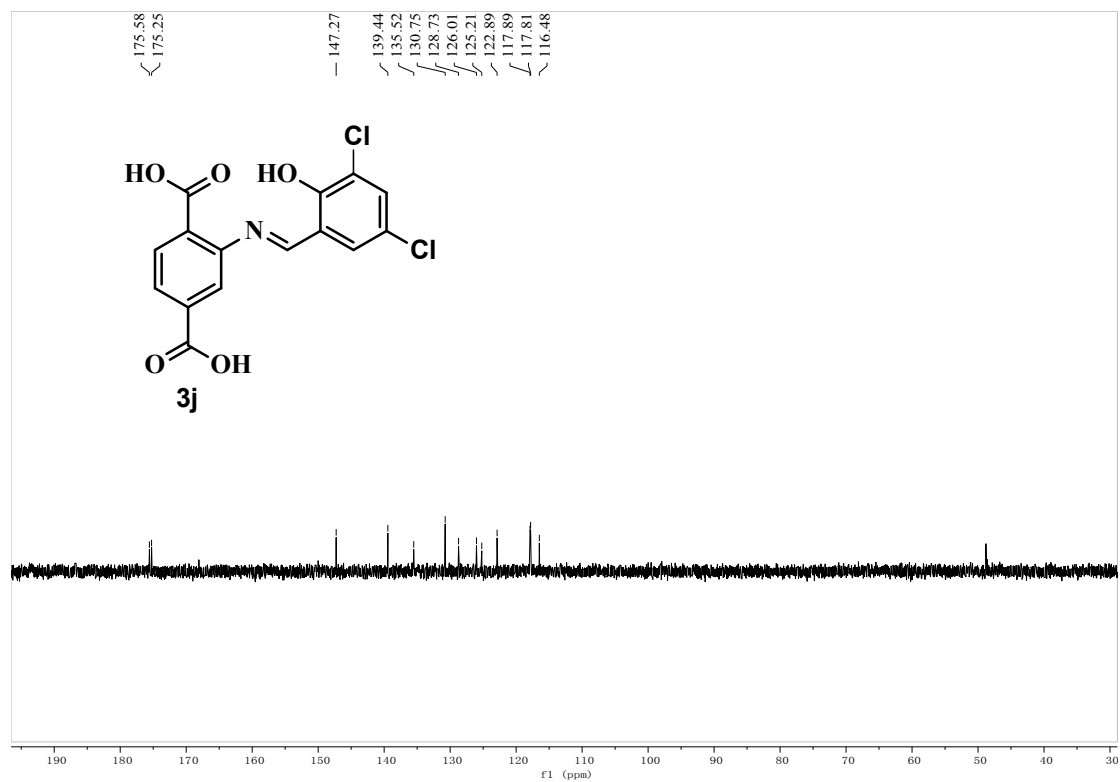
Figure S39: ^{13}C NMR (100 MHz, CD$_3$OD:D$_2$O 1:1) spectrum of product 3j.

3. Characterization of per-functionalized LMOFs.

Activation protocol

  All washed MOFs (with methanol then dried at 60 °C overnight) were degassed at 100 °C for 12 h under vacuum. In the case of IRMOF-3-**a**, FT-IR spectra were collected after heating at 80 °C for 3 h to confirm the removal of the guest and unreacted ligand prior to the N_2 sorption measurement at 77 K.
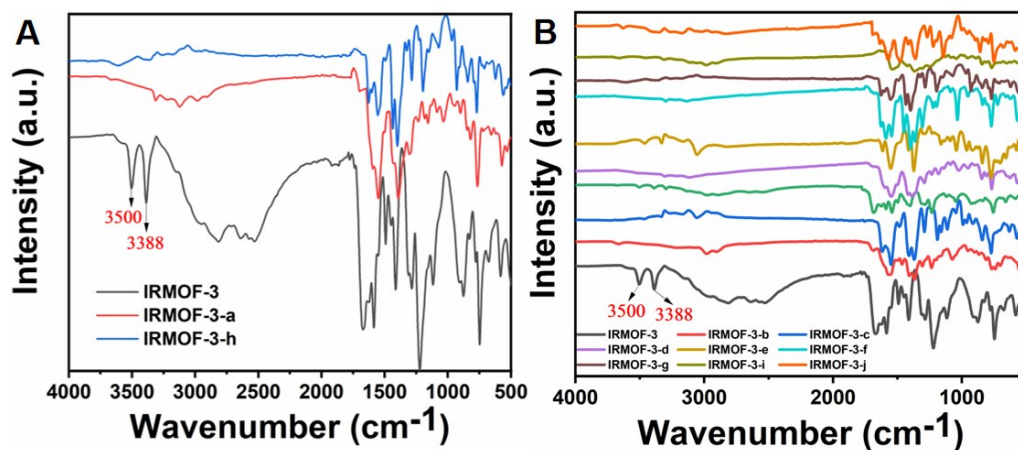
Figure S40: FT-IR spectra of IRMOF-3 and the others functionalized IRMOF-3.
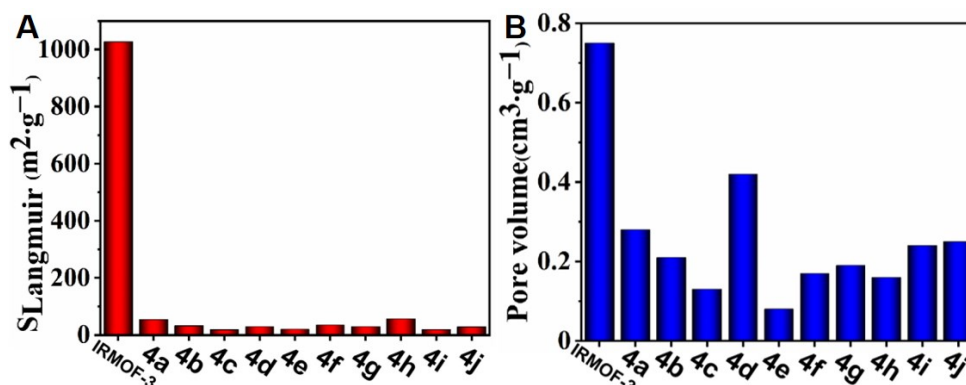
Figure S41: $S_{Langmuir}$ and pore volume of IRMOF-3 and functionalized LMOFs solid powder.
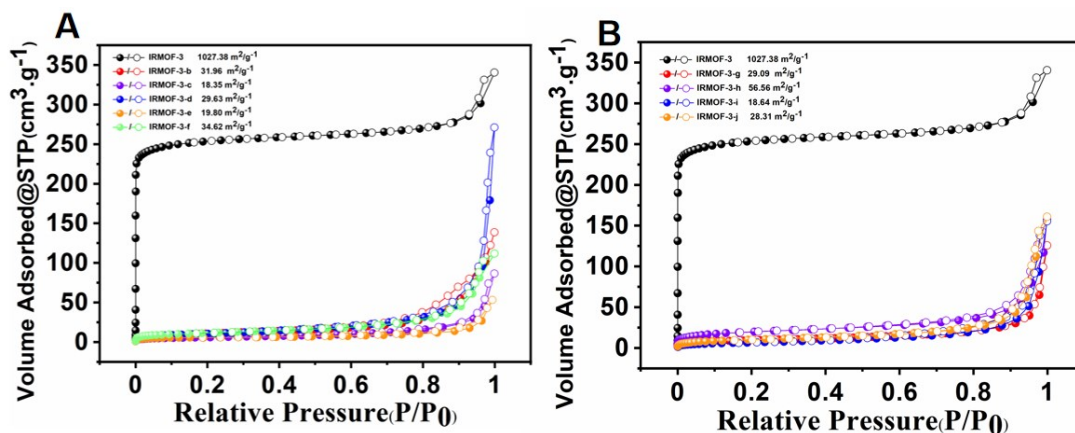
Figure S42: N_2 adsorption isotherm of IRMOF-3 and the others functionalized LMOFs.
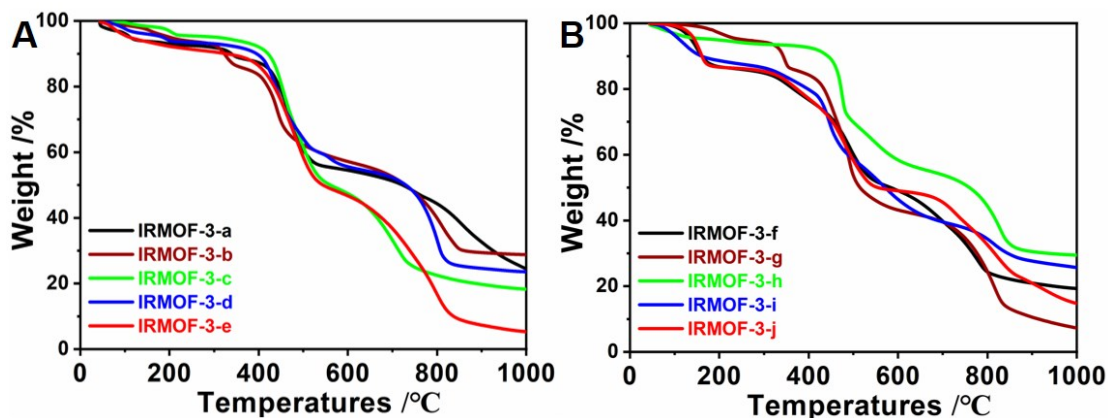
Figure S43: The Thermal gravimetric analysis (TGA) images of functionalized LMOFs.

Table S1. The FL properties of functionalized IRMOF-3.

Sample Code	λ_{ex}/nm	λ_{em}/nm	Color	FL	FLT/ns
IRMOF-3	355	580	yellow	yellow	0.6720
IRMOF-3-**a**	368	495	yellow	blue	1.1010
IRMOF-3-**b**	372	520	yellow	yellow	3.1647
IRMOF-3-**c**	368	492	yellow	blue	2.9267
IRMOF-3-**d**	378	581	orange	Orange	2.9858
IRMOF-3-**e**	372	497	khaki	yellow	3.1647
IRMOF-3-**f**	376	555	yellow	yellow	3.0611
IRMOF-3-**g**	371	495	yellow	green	3.5122
IRMOF-3-**h**	367	490	yellow	green	3.7710
IRMOF-3-**i**	373	533	yellow	yellow	3.5310
IRMOF-3-**j**	380	608	red	red	4.3326

4. TD-DFT theoretical calculations for Schiff-base 3a-3j.
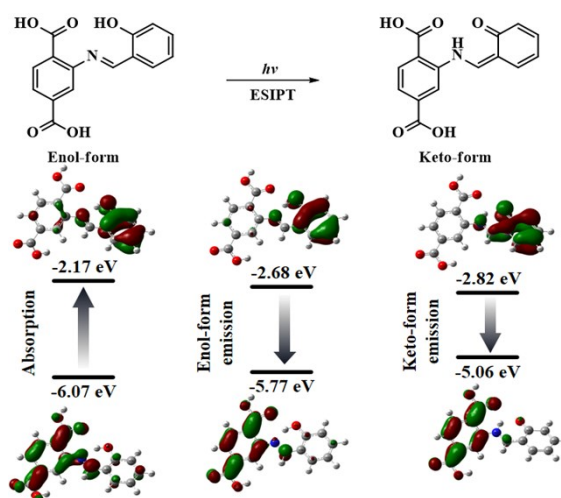
Figure S44. Molecular orbitals and energy levels of Schiff-bases **3a** in the ground (S_0) and excited (S_1) states calculated with TD-DFT at the level of B3LYP/6-31G* based on solvation of water.

Figure S45: Molecular orbitals and energy levels of Schiff-base **3b** in the ground (S_0) and excited (S_1) states for enol and keto forms calculated with TD-DFT at the level of B3LYP/6-31G* based on solvation of water.
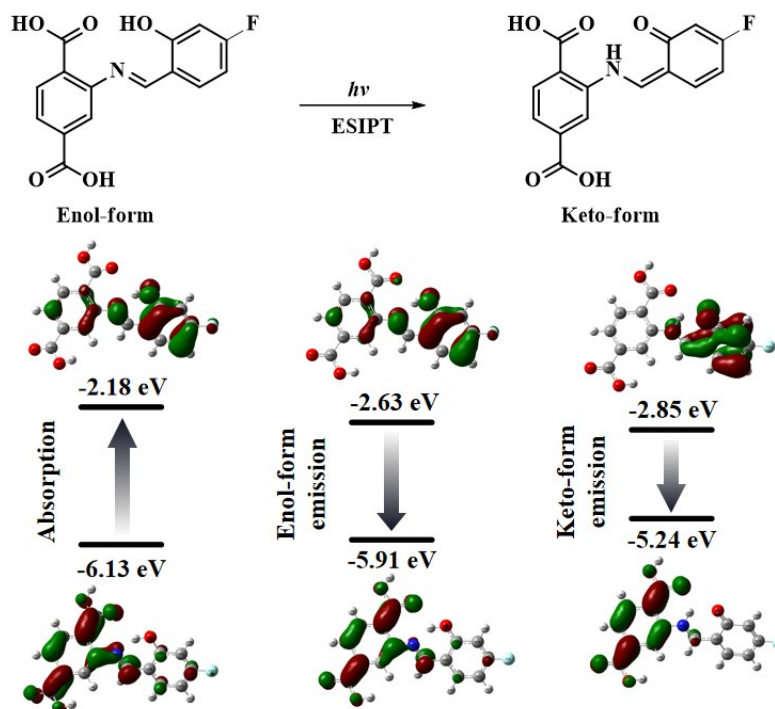
Figure S46: Molecular orbitals and energy levels of Schiff-base **3c** in the ground (S_0) and excited (S_1) states for enol and keto forms calculated with TD-DFT at the level of B3LYP/6-31G* based on solvation of water.
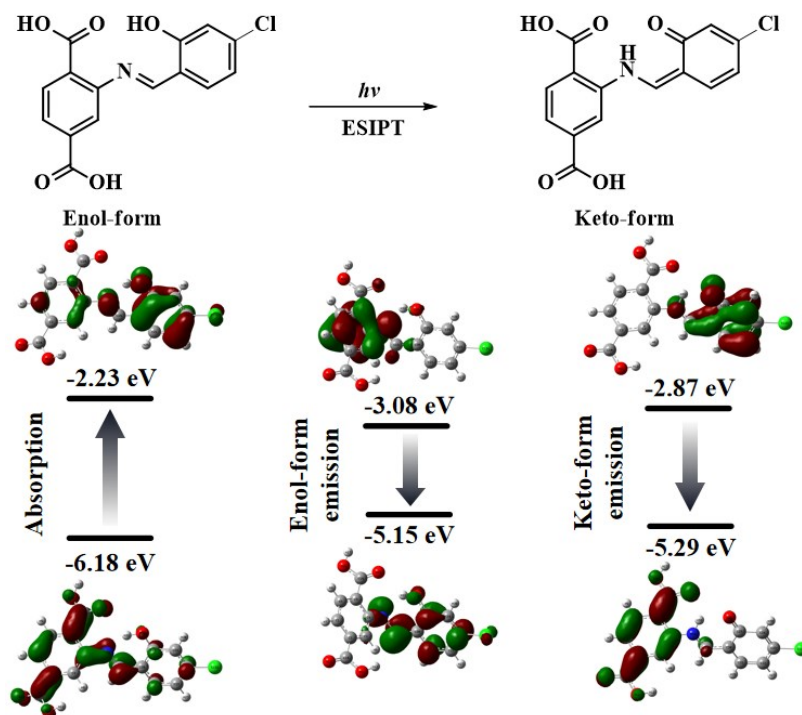
Figure S47: Molecular orbitals and energy levels of Schiff-base **3d** in the ground (S_0) and excited (S_1) states for enol and keto forms calculated with TD-DFT at the level of B3LYP/6-31G* based on solvation of water.
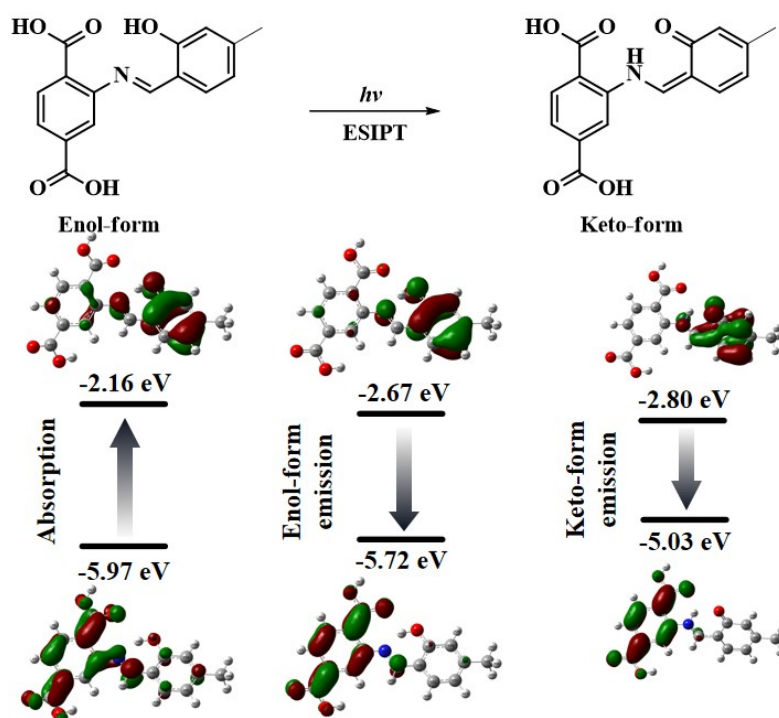
Figure S48: Molecular orbitals and energy levels of Schiff-base **3e** in the ground (S_0) and excited (S_1) states for enol and keto forms calculated with TD-DFT at the level of B3LYP/6-31G* based on solvation of water.
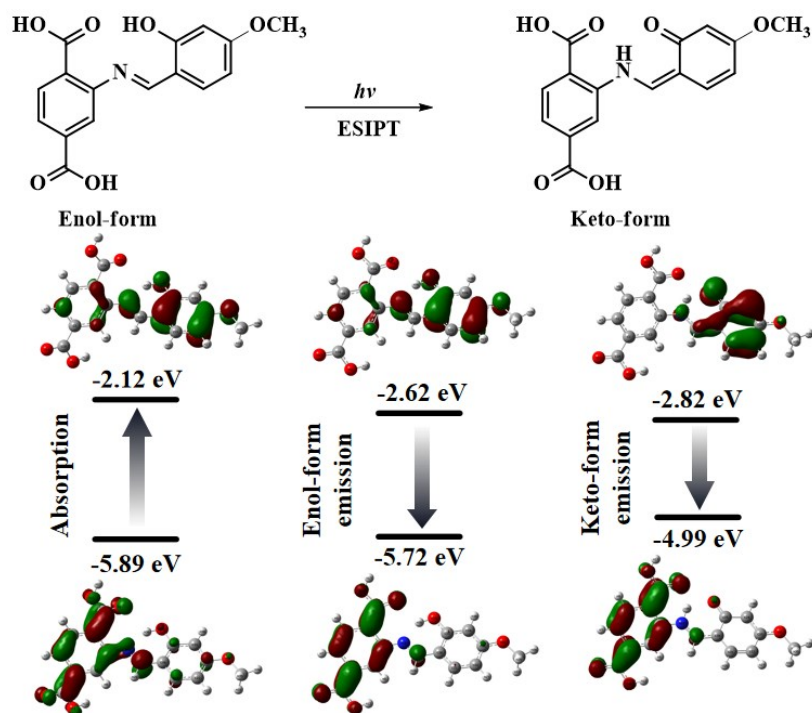
Figure S49: Molecular orbitals and energy levels of Schiff-base **3f** in the ground (S_0) and excited (S_1) states for enol and keto forms calculated with TD-DFT at the level of B3LYP/6-31G* based on solvation of water.
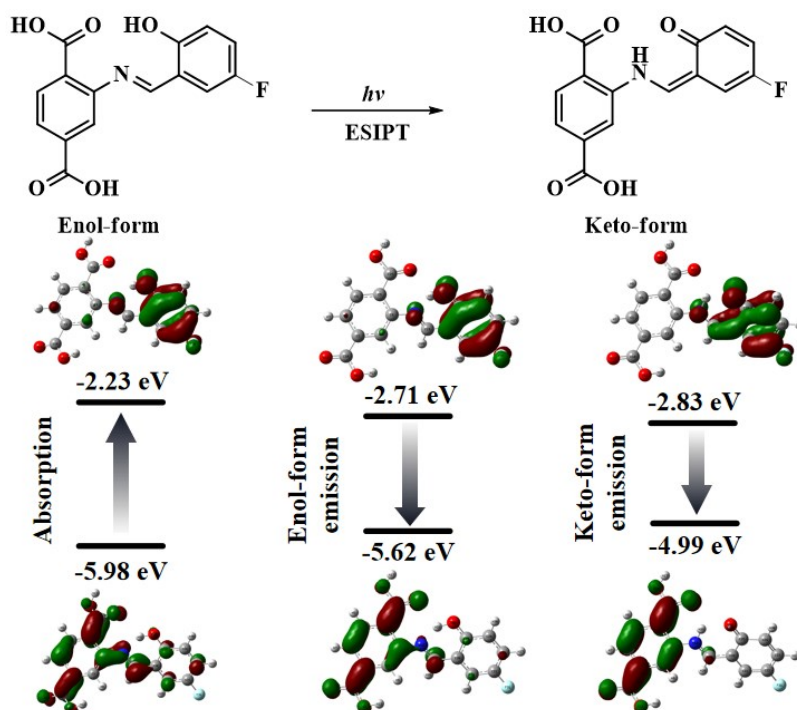
Figure S50: Molecular orbitals and energy levels of Schiff-base **3g** in the ground (S_0) and excited (S_1) states for enol and keto forms calculated with TD-DFT at the level of B3LYP/6-31G* based on solvation of water.
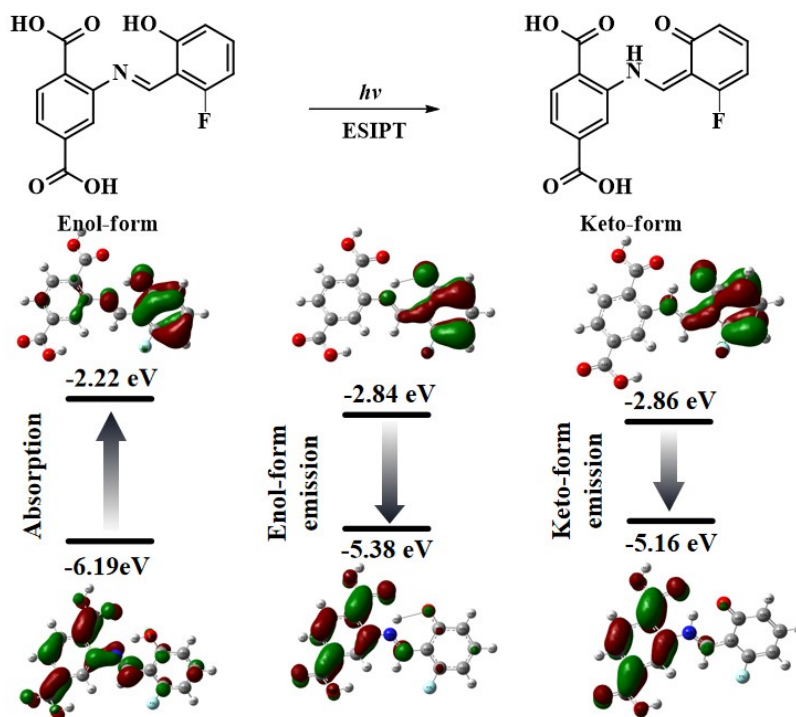
Figure S51: Molecular orbitals and energy levels of Schiff-base **3h** in the ground (S_0) and excited (S_1) states for enol and keto forms calculated with TD-DFT at the level of B3LYP/6-31G* based on solvation of water.
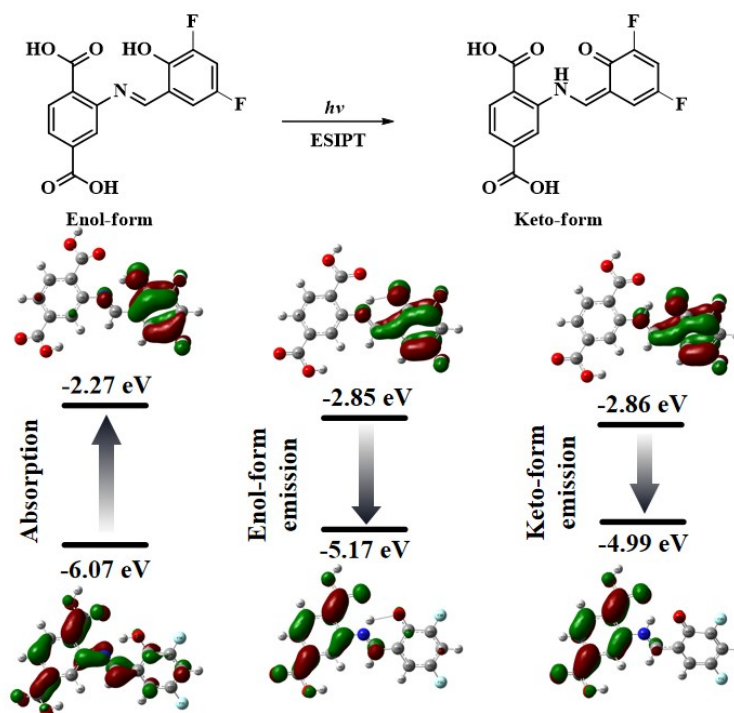
Figure S52: Molecular orbitals and energy levels of Schiff-base **3i** in the ground (S_0) and excited (S_1) states for enol and keto forms calculated with TD-DFT at the level of B3LYP/6-31G* based on solvation of water.
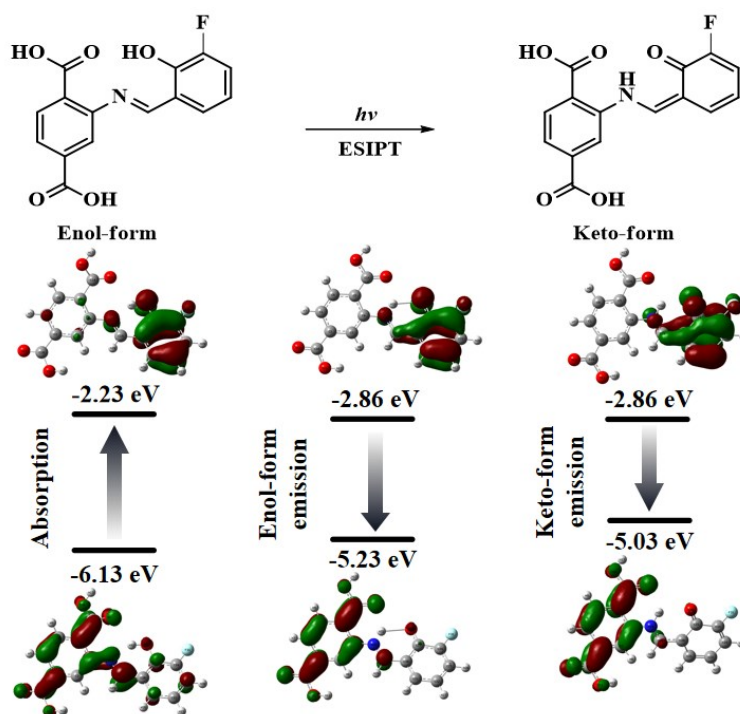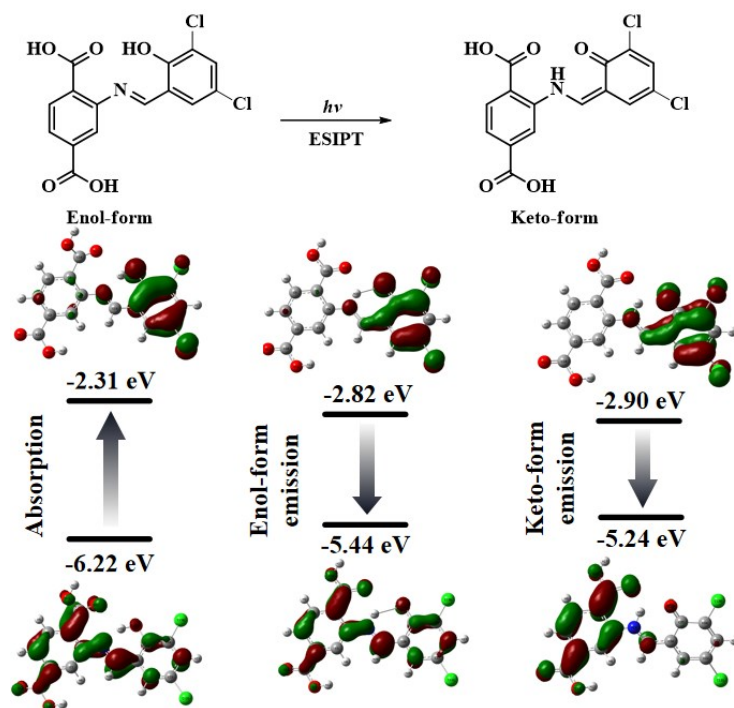
Figure S53: Molecular orbitals and energy levels of Schiff-base **3j** in the ground (S_0) and excited (S_1) states for enol and keto forms calculated with TD-DFT at the level of B3LYP/6-31G* based on solvation of water.

5. Molecular frontier orbitals and detail calculation data

Table S2 The frontier orbital energy levels of Enol-form, Keto-form, and the energy gap of Schiff-base **3a-3j**.[a]

AIEgens	Energy level (HOMO)	Energy level (LUMO)	Energy gap
Schiff-base **3a**	-6.07	-2.17	3.90
Enol-form	-5.77	-2.68	3.09
Keto-form	-5.06	-2.82	2.24
Schiff-base **3b**	-6.13	-2.23	3.90
Enol-form	-5.23	-2.86	2.37
Keto-form	-5.03	-2.86	2.17
Schiff-base **3c**	-6.13	-2.18	3.94
Enol-form	-5.91	-2.63	3.29
Keto-form	-5.24	-2.85	2.39
Schiff-base **3d**	-6.18	-2.23	3.95
Enol-form	-5.15	-3.08	2.07
Keto-form	-5.29	-2.87	2.42
Schiff-base **3e**	-5.97	-2.16	3.81
Enol-form	-5.72	-2.67	3.05
Keto-form	-5.03	-2.80	2.23
Schiff-base **3f**	-5.89	-2.12	3.77
Enol-form	-5.72	-2.62	3.10
Keto-form	-4.99	-2.82	2.18
Schiff-base **3g**	-5.98	-2.23	3.76
Enol-form	-5.62	-2.71	2.91
Keto-form	-4.99	-2.83	2.16
Schiff-base **3h**	-6.19	-2.22	3.96
Enol-form	-5.38	-2.84	2.53
Keto-form	-5.16	-2.86	2.31
Schiff-base **3i**	-6.07	-2.27	3.80
Enol-form	-5.17	-2.85	2.32
Keto-form	-4.99	-2.86	2.13
Schiff-base **3j**	-6.22	-2.31	3.90
Enol-form	-5.44	-2.82	2.62
Keto-form	-5.24	-2.90	2.34

[a] Calculated with TD-DFT at the level of B3LYP/6-31G* based on solvation of water, in which the vertical excitation as linear response solvation was used. S_{01}, S_{02} and S_{03} denoted the first and second vertical transition from S_0 state to S_1, S_2 and S_3 states, respectively, and f_{os} denoted oscillator strength of vertical transition.

Table S3 Calculation data of Schiff-base **3a-3j** in S_0 state.

AIEgen	States	Configurations	E (eV)	λ (nm)	f_{os}
Schiff-base **3a**	S_{01}	H→L(98.50%)	3.37	367.97	0.17
	S_{02}	H-2→L(13.53%),H-1→L(79.65%)	3.84	322.98	0.17
	S_{03}	H-2→L(12.27%),H→L+1(81.72%)	3.90	317.96	0.11
Schiff-base **3b**	S_{01}	H→L(98.13%)	3.38	366.97	0.15
	S_{02}	H-2→L(14.24%),H-1→L(79.47%)	3.72	333.00	0.24
	S_{03}	H-2→L(10.49%),H→L+1(82.51%)	3.85	322.11	0.06
Schiff-base **3c**	S_{01}	H→L(98.19%)	3.43	361.17	0.30
	S_{02}	H-4→L(3.20%),H-2→L(26.83%),H-1→L(63.37%)	3.83	324.08	0.10
	S_{03}	H-2→L(8.12%),H-1→L(9.30%),H→L+1(76.43%)	3.84	314.66	0.13
Schiff-base **3d**	S_{01}	H→L(98.08%)	3.44	360.69	0.36
	S_{02}	H-4→L(3.86%),H-2→L(26.64%),H-1→L(62.14%)	3.79	327.09	0.11
	S_{03}	H-2→L(5.44%),H-1→L(9.86%),H→L+2(78.14%)	3.92	316.00	0.10
Schiff-base **3e**	S_{01}	H→L(98.60%)	3.30	375.63	0.26
	S_{02}	H-2→L(15.55%),H-1→L(77.52%)	3.76	329.47	0.16
	S_{03}	H-2→L(11.19%),H→L+1(83.53%)	3.83	323.73	0.17
Schiff-base **3f**	S_{01}	H→L(97.85%)	3.29	377.04	0.37
	S_{02}	H-2→L(2.29%),H-1→L(88.47%),H-1→L+2(2.61%),H→L+2(3.91%)	3.73	332.39	0.04
	S_{03}	H-4→L(2.64%),H-2→L(27.13%),H-2→L+1(2.30%),H→L+1(64.19%)	3.83	323.71	0.38
Schiff-base **3g**	S_{01}	H→L(98.80%)	3.26	380.43	0.20
	S_{02}	H-2→L(16.4%),H-1→L(32.7%),H→L+2(46.87%)	3.76	329.88	0.21
	S_{03}	H-2→L(4.71%),H-1→L(41.38%),H→L+1(48.42%)	3.78	327.86	0.06
Schiff-base **3h**	S_{01}	H→L(97.81%)	3.44	360.60	0.19
	S_{02}	H-2→L(12.06%),H-1→L(82.16%)	3.73	332.58	0.23
	S_{03}	H-2→L(28.74%),H-1→L(3.24%),H→L+1(59.56%)	3.91	317.11	0.05
Schiff-base **3i**	S_{01}	H→L(98.66%)	3.29	376.60	0.15
	S_{02}	H-2→L(20.11%),H-1→L(72.43%)	3.74	331.46	0.22
	S_{03}	H-1→L(2.80%),H→L+1(92.78%)	3.81	325.26	0.06
Schiff-base **3j**	S_{01}	H→L(97.73%)	3.38	366.62	0.21
	S_{02}	H-4→L(2.30%),H-2→L(17.79%),H-1→L(74.02%)	3.75	330.76	0.20
	S_{03}	H-2→L(2.92%),H-1→L(2.53%),H→L+1(88.91%)	3.86	321.25	0.05

Table S4 Calculation data of Schiff-base **3a-3j** in S_1 state.

AIEgens	Form	Configurations	E (eV)	λ (nm)	f_{OS}
Schiff-base **3a**	Enol	H→L(98.59%)	2.54	487.53	0.1720
	Keto	H→L(99.82%)	1.77	700.53	0.0821
Schiff-base **3b**	Enol	H→L(99.79%)	1.89	654.47	0.1166
	Keto	H→L(99.84%)	1.71	724.00	0.0726
Schiff-base **3c**	Enol	H→L(98.69%)	2.71	457.14	0.3776
	Keto	H→L(99.80%)	1.91	648.46	0.0878
Schiff-base **3d**	Enol	H→L(98.74%)	1.09	1137.10	0.0015
	Keto	H→L(99.78%)	1.95	636.22	0.1026
Schiff-base **3e**	Enol	H→L(98.80%)	2.51	494.41	0.1931
	Keto	H→L(99.81%)	0.76	705.57	0.0812
Schiff-base **3f**	Enol	H→L(98.88%)	2.55	485.54	0.3604
	Keto	H→L(99.9%)	1.71	726.15	0.0738
Schiff-base **3g**	Enol	H→L(98.96%)	2.38	520.17	0.1458
	Keto	H→L(99.78%)	1.70	730.19	0.0882
Schiff-base **3h**	Enol	H→L(99.43%)	2.04	607.16	0.1448
	Keto	H→L(99.86%)	1.85	671.09	0.0826
Schiff-base **3i**	Enol	H→L(99.96%)	1.85	669.70	0.1463
	Keto	H→L(99.76%)	1.68	738.56	0.0824
Schiff-base **3j**	Enol	H→L(99.72%)	2.12	585.35	0.3028
	Keto	H→L(99.86%)	1.89	655.11	0.1246

Table S5 The specific bond lengths and dihedral angles of Schiff-base **3a** in S_0 and S_1 states. [a]
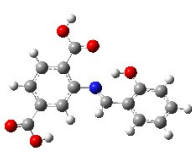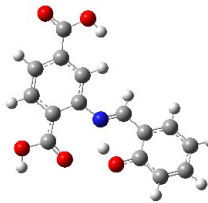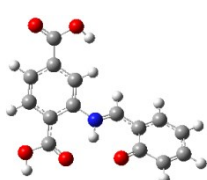
	Enol-form@S_0	Enol-form@S_1	Keto-form@S_1
O_{30}-H_{32}	0.998	1.055	/
N_{18}-O_{30}	2.647	2.529	2.739
C_3–C_4–N_{18}–C_{19}	140.510	-32.818	-38.414
C_4–N_{18}–C_{19}–C_{20}	177.062	177.028	176.812
N_{18}–C_{19}–C_{20}–C_{25}	2.867	3.669	-5.980
C_{19}–C_{20}–C_{25}–O_{30}	0.095	0.436	1.440
C_{20}–C_{25}–O_{30}–H_{32}	0.590	0.584	/

Table S6 The specific bond lengths and dihedral angles of Schiff-base **3b** in S_0 and S_1 states. [a]
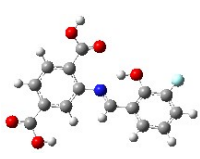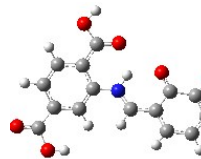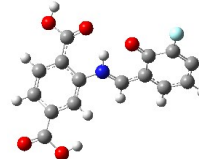
	Enol-form@S_0	Enol-form@S_1	Keto-form@S_1
O_{30}-H_{32}	1.002	/	/
N_{18}-O_{30}	2.632	2.773	2.760
C_3–C_4–N_{18}–C_{19}	-37.369	13.395	37.826
C_4–N_{18}–C_{19}–C_{20}	177.860	177.334	-176.429
N_{18}–C_{19}–C_{20}–C_{25}	3.681	-4.011	6.427
C_{19}–C_{20}–C_{25}–O_{30}	0.291	0.121	-1.653
C_{20}–C_{25}–O_{30}–H_{32}	0.176	/	/

Table S7 The specific bond lengths and dihedral angles of Schiff-base **3c** in S_0 and S_1 states. [a]
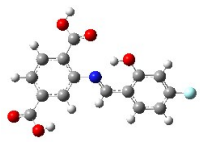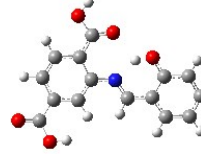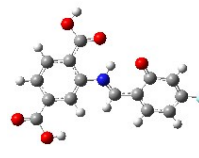
	Enol-form@S_0	Enol-form@S_1	Keto-form@S_1
O_{29}-H_{32}	1.003	1.027	/
N_{18}-O_{29}	2.626	2.583	2.749
C_3–C_4–N_{18}–C_{19}	38.387	26.491	36.925
C_4–N_{18}–C_{19}–C_{20}	-177.920	-176.011	-176.804
N_{18}–C_{19}–C_{20}–C_{25}	-3.277	-3.288	6.749
C_{19}–C_{20}–C_{25}–O_{29}	-0.182	-0.641	-0.974
C_{20}–C_{25}–O_{29}–H_{32}	-0.409	-1.484	/

Table S8 The specific bond lengths and dihedral angles of Schiff-base **3d** in S_0 and S_1 states.[a]
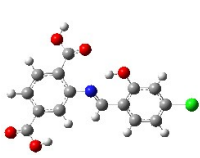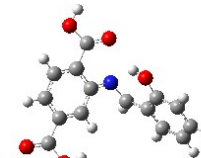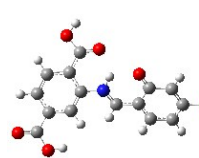
	Enol-form@S_0	Enol-form@S_1	Keto-form@S_1
O_{29}-H_{32}	1.003	0.982	/
N_{18}-O_{29}	2.629	2.796	2.748
C_3–C_4–N_{18}–C_{19}	38.420	-11.295	36.480
C_4–N_{18}–C_{19}–C_{20}	-177.922	-95.808	-176.088
N_{18}–C_{19}–C_{20}–C_{25}	-3.577	-1.814	7.030
C_{19}–C_{20}–C_{25}–O_{29}	-0.278	-3.200	-1.361
C_{20}–C_{25}–O_{29}–H_{32}	-0.347	-10.911	/

Table S9 The specific bond lengths and dihedral angles of Schiff-base **3e** in S_0 and S_1 states. [a]

	Enol-form@S_0	Enol-form@S_1	Keto-form@S_1
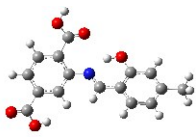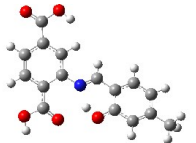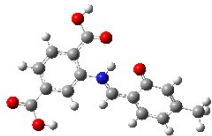
O_{29}-H_{35}	1.001	1.038	/
N_{18}-O_{29}	2.634	2.557	2.740
C_3–C_4–N_{18}–C_{19}	-38.488	-34.734	39.374
C_4–N_{18}–C_{19}–C_{20}	177.757	177.580	-176.691
N_{18}–C_{19}–C_{20}–C_{25}	3.140	4.386	5.769
C_{19}–C_{20}–C_{25}–O_{29}	-0.214	0.660	-1.402
C_{20}–C_{25}–O_{29}–H_{35}	0.452	0.624	/

Table S10 The specific bond lengths and dihedral angles of Schiff-base **3f** in S_0 and S_1 states.[a]
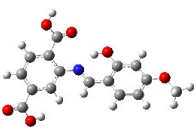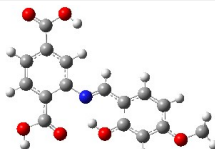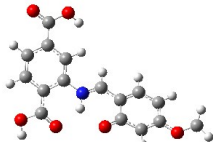
	Enol-form@S_0	Enol-form@S_1	Keto-form@S_1
O_{29}-H_{36}	1.002	1.011	/
N_{18}-O_{29}	2.632	2.616	2.779
C_3–C_4–N_{18}–C_{19}	-36.967	-32.100	-32.340
C_4–N_{18}–C_{19}–C_{20}	177.813	177.116	174.608
N_{18}–C_{19}–C_{20}–C_{25}	2.806	5.119	-6.420
C_{19}–C_{20}–C_{25}–O_{29}	0.183	0.838	0.246
C_{20}–C_{25}–O_{29}–H_{36}	0.535	1.140	/

Table S11 The specific bond lengths and dihedral angles of Schiff-base **3g** in S_0 and S_1 states.[a]
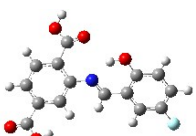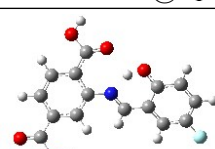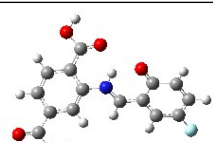
	Enol-form@S_0	Enol-form@S_1	Keto-form@S_1
O_{29}-H_{32}	1.000	1.054	/
N_{18}-O_{29}	2.635	2.529	2.725
C_3–C_4–N_{18}–C_{19}	38.784	32.965	40.447
C_4–N_{18}–C_{19}–C_{20}	-178.075	-176.500	-175.890
N_{18}–C_{19}–C_{20}–C_{25}	-3.508	-4.117	5.726
C_{19}–C_{20}–C_{25}–O_{29}	-0.054	-0.675	-2.091
C_{20}–C_{25}–O_{29}–H_{32}	-0.492	-0.186	/

Table S12 The specific bond lengths and dihedral angles of Schiff-base **3h** in S_0 and S_1 states.[a]

	Enol-form@S_0	Enol-form@S_1	Keto-form@S_1
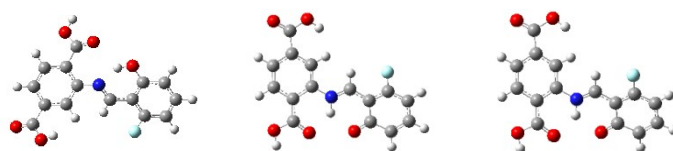
O$_{29}$-H$_{32}$	1.002	/	/
N$_{18}$-O$_{29}$	2.626	2.755	2.751
C$_3$–C$_4$–N$_{18}$–C$_{19}$	39.009	24.881	34.527
C$_4$–N$_{18}$–C$_{19}$–C$_{20}$	-178.195	-176.011	-175.962
N$_{18}$–C$_{19}$–C$_{20}$–C$_{25}$	-3.732	5.300	6.965
C$_{19}$–C$_{20}$–C$_{25}$–O$_{29}$	0.136	-0.627	-1.784
C$_{20}$–C$_{25}$–O$_{29}$–H$_{32}$	-0.332	/	/

Table S13 The specific bond lengths and dihedral angles of Schiff-base **3i** in S$_0$ and S$_1$ states.[a]

	Enol-form@S$_0$	Enol-form@S$_1$	Keto-form@S$_1$
O$_{29}$-H$_{32}$	1.001	/	/
N$_{18}$-O$_{29}$	2.637	2.771	2.750
C$_3$–C$_4$–N$_{18}$–C$_{19}$	39.529	24.645	39.082
C$_4$–N$_{18}$–C$_{19}$–C$_{20}$	-178.064	-176.730	-176.707
N$_{18}$–C$_{19}$–C$_{20}$–C$_{25}$	-3.800	3.045	5.892
C$_{19}$–C$_{20}$–C$_{25}$–O$_{29}$	-0.213	-0.122	-1.304
C$_{20}$–C$_{25}$–O$_{29}$–H$_{32}$	-0.372	/	/

Table S14 The specific bond lengths and dihedral angles of Schiff-base **3j** in S$_0$ and S$_1$ states.[a]

	Enol-form@S$_0$	Enol-form@S$_1$	Keto-form@S$_1$
O$_{29}$-H$_{36}$	1.006	/	/
N$_{18}$-O$_{29}$	2.617	2.757	2.749
C$_3$–C$_4$–N$_{18}$–C$_{19}$	-38.162	-14.491	33.189
C$_4$–N$_{18}$–C$_{19}$–C$_{20}$	177.796	176.167	-177.075
N$_{18}$–C$_{19}$–C$_{20}$–C$_{25}$	3.616	-6.481	7.483
C$_{19}$–C$_{20}$–C$_{25}$–O$_{29}$	0.342	-0.416	-0.595
C$_{20}$–C$_{25}$–O$_{29}$–H$_{36}$	-0.003	/	/

[a] Calculated with TD-DFT at the level of B3LYP/6-31G* based on solvation of water. The units of bond lengths and dihedral angles are Å and degree, respectively.
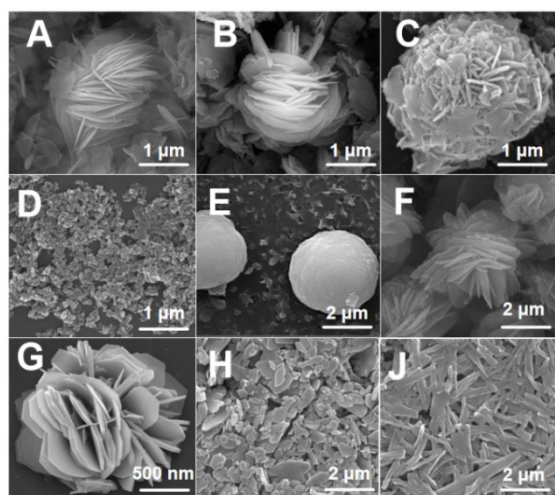
Figure S54: The FESEM images of (A) IRMOF-3-**b**, (B) IRMOF-3-**c**, (C) IRMOF-3-**d**, (D) IRMOF-3-**e**, (E) IRMOF-3-**f**, (F) IRMOF-3-**g**, (G) IRMOF-3-**h**, (H) IRMOF-3-**i**, (J) IRMOF-3-**j**. Scale bars correspond to 1-2μm.

Table S15 The change in energy after formation to J-aggregate.

Molecule	Energy(kJ/mol)
3a	-24.32
3b	-19.74
3c	-20.72
3d	-20.30
3e	-21.97
3f	-20.96
3g	-23.05
3h	**-25.92**
3i	-21.19
3j	-22.74

6. Detection of Cu^{2+} and thiols by the functional IRMOF-3.

6.1 Detection of Cu^{2+} by IRMOF-3-h

20 μL of 100 μM of thirteen different ions (Cu^{2+}, Cd^{2+}, Pb^{2+}, Mn^{2+}, Co^{2+}, Ni^{2+}, Ca^{2+}, Mn^{2+}, Mg^{2+}, Zn^{2+}, Ag^+, SO_4^{2-}, Cl^-, S^{2-}) and Leucine (Leu), Lysine (Lys) and Serine (Ser) were added into 2 mL of IRMOF-3-**h** (5 μg·mL^{-1}) aqueous solution respectively, and then the fluorescence spectra of the mixture were recorded after 1 min. To study the detection range of Cu^{2+}, 2 mL of LMOF aqueous dispersing agent was added to a 3 mL quartz cell, 10 μL of Cu^{2+} solutions with varied concentrations (0.2 to 200 μM) were added to the system. The fluorescence spectra were also recorded (excited at 367 nm) after 1 min.

Analysis of practical water sample was carried out to evaluate the viability and practicality of the developed LMOF sensor. River water samples were collected from Yudai River of Changsha (China). In order to eliminate the matrix effect, the obtained real water samples were filtered through 0.22 μM filter membrane, and then diluted 10-fold with ultrapure water. To the samples of river water were added standard Cu^{2+} solutions with different concentrations (0, 1, 2, and 3 nM) respectively, which were analyzed by the IRMOF-3-**h** sensor. The fluorescence intensity was recorded (excited at 367 nm) after 1 min.

In comparison with other reported FL methods[1-15], this sensing approach also shows higher sensitivity (1 or 2 orders of magnitude decrease in LOD) for the detection of Cu^{2+} (Table S17). The highly sensing sensitivity can be attributed to the precursors AIE-active Schiff-bases assembled in the frame of functional IRMOF-3.

Table S16 Various sensing strategies for the detection of Cu^{2+}.

Methods	Probe material	LOD(nM)	Real samples	References
Colorimetric	Triazole-linked fluorescein lactone	200	Naked-eye detection	[1]
Colorimetric	CdS QDs	5.3	River water	[2]
SERS	AuNP-AgNP	0.18	River water	[3]
Electrochemical	ZnO/CdS	10	River water	[4]
Click chemistry	G-quadruplex	5.9	Tap water	[5]
Fluorescence	Luminol-Tb-GMP CPNPs	4.2	River water	[6]
Fluorescence	H39GFP	50	Serum	[7]
Fluorescence	Graphene foam	0.6	Serum	[8]
Fluorescence	CDs	300	Rat brain	[9]
Fluorescence	CDs@Eu-DPA MOFs	26.3	Drinking water	[10]
Fluorescence	AIE molecule	9.12	---	[11]
Fluorescence	Molecule probe	261	Spring water	[12]
Fluorescence	Nanoparticle	10	Industrial wastewater	[13]
Fluorescence	PSM LMOFs	2.6	Tap water	[14]
Fluorescence	LMOF-2	0.55	River water	[15]
Fluorescence	Functional IRMOF-3	0.135	River water	This work

6.2 The application of LMOF in detection Cu^{2+}

Table S17 Determination of Cu^{2+} in river water samples.

Samples	No.	Added (nM)	Found (nM)	Recovery (%)	RSD (%) (n=3)
Xiangjiang River Of Changsha	1	0	2.329	-	0.18
	2	1	3.351	102.2	0.26
	3	2	4.293	98.5	0.33
	4	3	5.340	100.4	0.24

The river water sample were filtered and diluted 10-fold with ultrapure water. ICP-MS characterization proved that the concentration of Cu^{2+} in the sample to be tested was 0.001 mg/L (17.5 nM), which was basically consistent with the result of fluorescent probe detection.

$$Y = 0.8579 + \frac{-230.4112}{1 + e^{\frac{X + 532.0236}{92.2410}}}$$

6.3 The detection of IRMOF-3-h/Cu^{2+} complex in detection biothiol.

2 mL of LMOF/Cu^{2+} aqueous dispersing agent was added to a 3 mL quartz cell. As for the detection of biothiol (Cys, Hcy and GSH), 10 μL of biothiol solutions with varied concentrations (2 to 200 μM) were added to IRMOF-3-**h**/Cu^{2+} complex. The fluorescence spectra were recorded (excited at 367 nm) after 1 min.

The fluorescent probes of IRMOF-3-**h**/Cu^{2+} complex (50 μg·mL^{-1} IRMOF-3-**h** and 50 μM Cu^{2+}) with the addition of different biomolecules (Cys, Hcy, GSH, AA, Met, Phe, Try and Tys) and anion ions (S^{2-} and $H_2PO_4^-$) were studied. As shown in Figure S54A, the quenched FL intensity could be recovered by adding biothiol (Cys, Hcy and GSH) into the system of IRMOF-3-**h**/Cu^{2+}. Only in the presence of biothiol (Cys, Hcy and GSH), a significant increase in fluorescence intensity was observed and the intensity was recovered to 73.1%, 65.2% and 35.3%, the LOD of GSH, Cys and Hcy was calculated as 0.63, 1.95 and 0.22 nM based on the equation 3σ/S, respectively. Due to the large ring tension formed by Hcy coordination with copper, the response of Hcy was in fact smaller than that of Cys and GSH.
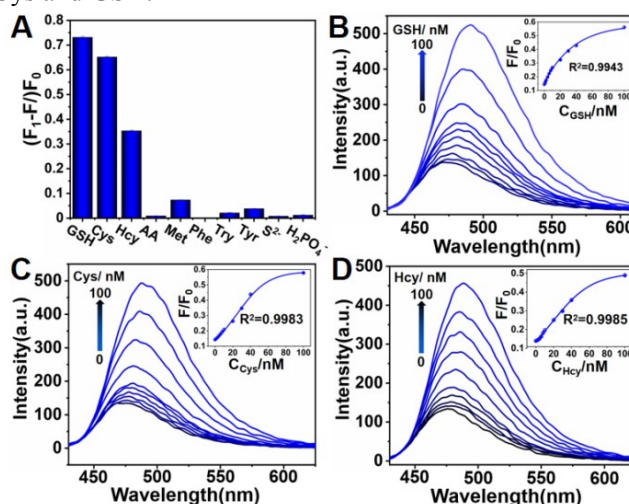

Figure S55. (A) Comparison of FL intensities of IRMOF-3-**h**/Cu^{2+} upon addition of different amino acids and anion ions all at the concentrations of 1 μM. (B) Plot of the FL intensity as a function of GSH concentration. (C) Cys concentration. (D) Hcy concentration. Exposed to various concentrations of GSH, Cys and Hcy: 0, 1, 2, 4, 6, 8, 10, 20, 30, 40, 100 nM from bottom to top.

6.4 FTSEM characterization and mechanism verification.

It is worth mentioning that when copper ions bonded with LMOF, the flower-like structure was destroyed. However, as the biothiol was added, the flower-like morphology was recovered, and organic molecules were obviously attached to the surface (Figure S55). Meanwhile, the energy dispersive X-ray spectrum (EDS) showed that C, O, N, S and Zn elements were uniformly distributed on the surface of LMOF recovered by adding thiols.
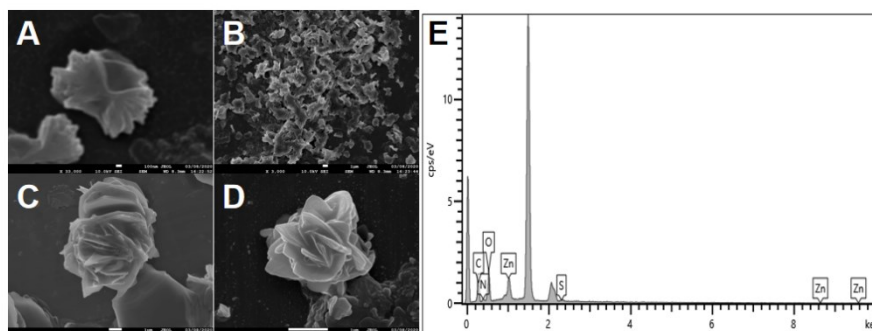

Figure S56: FESEM images of (A),(B) IRMOF-3-**h** reacts with copper ions. (C),(D) IRMOF-3-**h**/Cu^{2+} complex recovered by adding thiols. (E) the energy dispersive X-ray spectrum (EDS) of IRMOF-3-**h**/Cu^{2+} complex recovered by adding thiols.
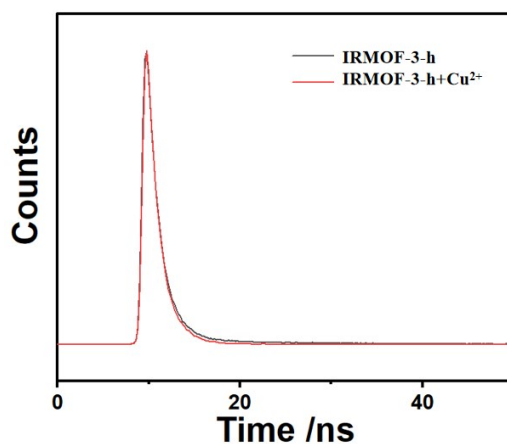

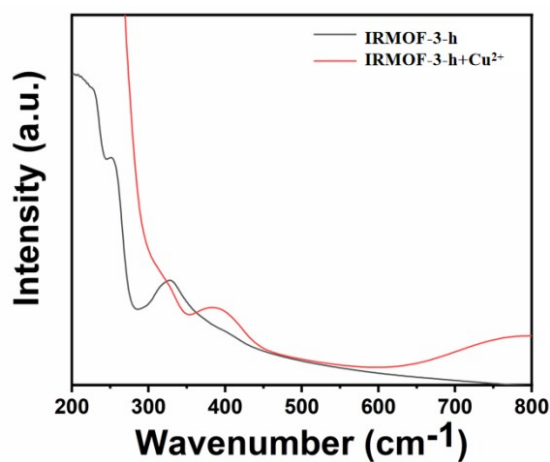Figure S57: The time-resolved fluorescence decay of IRMOF-3-**h** and IRMOF-3-**h**+Cu^{2+}.

Figure S58: The UV-vis absorption spectrum of IRMOF-3-**h** and IRMOF-3-**h**+Cu^{2+}.

References

1. Y. B. Ruan, C. Li, J. Tang and J. Xie, *Chem Commun (Camb)*, 2010, **46**, 9220-9222.

2. S. Tang, M. Wang, Z. Li, P. Tong, Q. Chen, G. Li, J. Chen and L. Zhang, *Biosens Bioelectron*, 2017, **89**, 866-870.

3. Y. Wang, Z. Su, L. Wang, J. Dong, J. Xue, J. Yu, Y. Wang, X. Hua, M. Wang, C. Zhang and F. Liu, *Anal Chem*, 2017, **89**, 6392-6398.

4. Q. Shen, X. Zhao, S. Zhou, W. Hou and J.-J. Zhu, *The Journal of Physical Chemistry C*, 2011, **115**, 17958-17964.

5. C. Ge, Q. Luo, D. Wang, S. Zhao, X. Liang, L. Yu, X. Xing and L. Zeng, *Anal Chem*, 2014, **86**, 6387-6392.

6. Y.-J. Tong, L.-D. Yu, L.-L. Wu, S.-P. Cao, Y.-L. Guo, R.-P. Liang and J.-D. Qiu, *ACS Sustainable Chemistry & Engineering*, 2018, **6**, 9333-9341.

7. C. Lei, Z. Wang, Z. Nie, H. Deng, H. Hu, Y. Huang and S. Yao, *Anal Chem*, 2015, **87**, 1974-1980.

8. X. Fang, Y. Liu, L. Jimenez, Y. Duan, G. B. Adkins, L. Qiao, B. Liu and W. Zhong, *Anal Chem*, 2017, **89**, 11758-11764.

9. Y. Lin, C. Wang, L. Li, H. Wang, K. Liu, K. Wang and B. Li, *ACS Appl Mater Interfaces*, 2015, **7**, 27262-27270.

10. J. Hao, F. Liu, N. Liu, M. Zeng, Y. Song and L. Wang, *Sensors and Actuators B: Chemical*, 2017, **245**, 641-647.

11. J. Yang, J. Chai, B. Yang and B. Liu, *Spectrochim Acta A Mol Biomol Spectrosc*, 2019, **211**, 272-279.

12. W. Lin, L. Long, B. Chen, W. Tan and W. Gao, *Chem Commun (Camb)*, 2010, **46**, 1311-1313.

13. C. Zong, K. Ai, G. Zhang, H. Li and L. Lu, *Anal Chem*, 2011, **83**, 3126-3132.

14. X. L. Yang, C. Ding, R. F. Guan, W. H. Zhang, Y. Feng and M. H. Xie, *J Hazard Mater*, 2021, **403**, 123698.

15. S. Xie, Q. Liu, F. Zhu, M. Chen, L. Wang, Y. Xiong, Y. Zhu, Y. Zheng and X. Chen, *Journal of Materials Chemistry C*, 2020, **8**, 10408-10415.